# ANALYSIS OF THERMAL DRIFT IN ATOMIC FORCE MICROSCOPY AND DESIGN OF COMPENSATING MEMS-BASED MICRO-STAGE

by

Selin Tolunay

B.S., Electronics Engineering, Sabancı University, 2010

Submitted to the Institute for Graduate Studies in
Science and Engineering in partial fulfillment of
the requirements for the degree of
Master of Science

Graduate Program in Electrical and Electronics Engineering

Boğaziçi University

2012

# ACKNOWLEDGEMENTS

First and foremost, I would like to express my appreciation to my thesis advisor, Assist. Prof. Hamdi Torun for his guidance and support throughout my research and thesis. With his knowledge and experience in the field of microsystems it became possible for me to reach Master of Science. Being a member of Bio-AFM Laboratory under the supervision of Assist. Prof. Torun was always a pleasure for me. I would like to thank Assist. Prof. Arda Deniz Yalçınkaya and Assoc. Prof. Hakan Ertürk for sharing their knowledge and taking part in my thesis jury. I would like to also sincerely thank Assist. Prof. Yalçınkaya and Assoc. Prof. Şenol Mutlu for giving me a chance to use their laboratories (MNL and BU-MEMS) during the optical setup experiments and fabrication process trials and giving me advice. I am deeply appreciated with my research partner, Semih Sevim for his help, support, motivation and friendship in this work. Without him it would be much more difficult to achieve. Together with him I would like to thank Mustafa Kemal Ruhi and Mehmet Yumak for their help and support during the fabrication process in clean room for three months. I would like to give my acknowledgement to Microsystem Based Medical Device Development Center of Bogazici University Life Sciences and Research Center where all the fabrication was performed. I would also like to thank Assist. Prof. Ahmet Öncü for giving me a lab-space in his laboratory (RFIC) as our laboratory was under construction.

I owe many thanks to my dearest colleagues from Bogazici University for their friendship, support and encouragement; Tayyar Oğuz Karaduman, Uraz Çakacı, İsmail Kara, Can Doğa Kırbaç, Berk Çamlı, Ali Murat Gök, Simge Ay, Berk Omuz, Berkan Yaman, İsmail Terkeşli, Aida Sadeghzadeh, Doğan Ulus, Vahap Barış Esen, Gökhan Hacıahmetoğlu, Bilgiday Yüce, Cihan Alkan, Demet Yüksel and Tina Seifpoor. Even one cup of coffee or a lunch with them was my motivation for this thesis. I would like to also thank Baykal Sarıoğlu, İskender Haydaroğlu, Gürkan Sönmez, Okan Z. Batur, Umut Çindemir, Betül Küçükakarsu Usta, F. Melih Akçakaya, Seyrani Korkmaz and Engin Afacan from Beta-Lab for their friendship and helping me to overcome the complications during my research.

Last but not least, I give my deepest love and appreciation to the special people that I am happy for having in my life, but especially to my dearest parents for their unconditional love and emotional support during my graduate study in Bogazici.

This research is supported under “Marie Cruie Actions - IRG, Project Number 276937”.

# ABSTRACT


## ANALYSIS OF THERMAL DRIFT IN ATOMIC FORCE MICROSCOPY AND DESIGN OF COMPENSATING MEMS-BASED MICRO-STAGE

Single-molecule force spectroscopy has become a powerful research area. The most commonly used single-molecule force spectroscopy techniques are optical tweezers, magnetic tweezers and atomic force microscopy (AFM). For accuracy of the experiments in all three techniques, the ability to measure the position of the probe is critical. Thermal drift in the experimental setup is detrimental for the stability and accuracy of measurements. Temperature fluctuation in an AFM setup causes cantilever deflection. For long time scale experiments in AFM, ambient temperature stability becomes the main concern as AFM cantilever is usually a bimaterial structure and sensitive to temperature gradient. Thermal drift in AFM can be harmful for biomolecules anchored between a cantilever and a stationary sample surface as the force on the molecules increases if the cantilever deflects towards the surface. In addition, thermally induced deflection causes false force readings and a shift in zero-force level. In this thesis, the analysis of thermal drift in AFM cantilevers by thermal drift modeling and experimental characterization of the thermal drift in AFM cantilever is reported. With MEMS technology, various thermomechanically matched micro-stages in order to compensate the thermal drift in AFM cantilevers are designed. Lastly, fabrication process for the MEMS micro-stages, which is a 3-mask process, is developed.

# ÖZET

## ATOMIK KUVVET MIKROSKOBUNDA GÖZLENEN ISIL SAPMANIN ANALIZI VE SAPMA ÖNLEYİCİ MİKRO-YAPI TASARIMI

Tek-molekül kuvvet spektroskopisi güçlü bir araştırma alanı haline gelmiştir. En sık kullanılan tek-molekül kuvvet spektroskopisi teknikleri optik cımbız, manyetik cımbız ve atomik kuvvet mikroskobudur. Her üç teknikte de deneylerdeki hassasiyet sondanın pozisyonunu ölçmek için kritik önem taşır. Deneysel kurulumdaki ısıl kayma ölçümlerinin kararlılığı ve doğruluğu için zararlıdır. AFM kurulumunda oluşacak sıcaklık dalgalanması manivelanın bükülmesine neden olur. AFM'deki uzun zaman ölçekli deneyler için ortam sıcaklığındaki istikrarın kritik olması AFM manivelanın genellikle bimateryal yapıda ve sıcaklık değişimine karşı hassas olmasındandır. AFM'deki ısıl sapma bir manivela ve sabit bir örnek yüzeyi arasında sabitlenmiş bulunan biyomoleküller için, manivela yüzeye doğru büküldüğü takdirde moleküller üzerine gelen kuvvet artacağından, zararlı olabilir. Buna ek olarak, ısının neden olduğu bükülme yanlış kuvvet okumalarına ve sıfır kuvvet düzeyinde kaymaya neden olur. Bu tezde, AFM manivelalarındaki ısıl sapmanın ısıl sapma modellemesiyle analizi ve AFM manivelalarındaki ısıl sapmanın deneysel karakterizasyonu raporlanmaktadır. AFM manivelalarındaki ısıl sapmanın önlenmesi için manivela ile termomekanik olarak eş olan çeşitli mikroyapılar MEMS teknolojisi ile tasarlanmaktadır. Son olarak, üretiminde 3 kat maske kullanılan MEMS mikroyapılar için üretim aşamaları geliştirilmiş.

# TABLE OF CONTENTS

# LIST OF FIGURES

# LIST OF TABLES

# LIST OF SYMBOLS

| | |
|---|---|
| $A$ | Area |
| $c$ | Heat capacity |
| $C$ | Capacitance |
| $E$ | Young's modulus |
| $E^*$ | Equivalent Young's modulus of bimaterial cantilever |
| $E_1$ | Young's modulus of first layer |
| $E_2$ | Young's modulus of second layer |
| $F$ | Force |
| $h$ | Convective heat transfer coefficient |
| $h_1$ | Thickness of cantilever's first layer |
| $h_2$ | Thickness of cantilever's second layer |
| $H$ | Thickness of cantilever |
| $I$ | Inertia |
| $k$ | Stiffness |
| $k_{cond}$ | Thermal conductivity |
| $K$ | Coefficient |
| $L$ | Length of cantilever |
| $m$ | Mass |
| $n$ | Thickness ratio |
| $\frac{1}{R}$ | Radius of curvature of cantilever |
| $Q$ | Quality factor |
| $R_{cond}$ | Thermal resistance for conduction |
| $R_{conv}$ | Thermal resistance for convection |
| $S$ | Deflection sensitivity |
| $S_T$ | Sensitivity |
| $\tau$ | Time constant of the cantilever's tip |
| $t_{rise}$ | Rise time of the cantilever's tip |
| $V_x$ | Cantilever's deflection in volt |

| | |
|---|---|
| $V$ | Volume |
| $W$ | Width of cantilever |
| $x$ | Deflection of the cantilever |
| | |
| $\alpha_1$ | Coefficient of thermal expansion for first layer |
| $\alpha_2$ | Coefficient of thermal expansion for second layer |
| $\Delta T$ | Temperature change |
| $\phi$ | Young's modulus ratio |
| $\rho$ | Density |

# LIST OF ACRONYMS/ABBREVIATIONS

| | |
|---|---|
| 3D | Three Dimensional |
| AFM | Atomic Force Microscopy |
| FEM | Finite Element Model |
| IC | Integrated Circuit |
| IPA | Isopropyl alcohol |
| PR | Photoresist |
| STM | Scanning Tunneling Microscope |
| TEC | Thermoelectric cooler |

# 1. INTRODUCTION

Single-molecule force spectroscopy has become a powerful research area. The most commonly used single-molecule force spectroscopy techniques shown in Figure 1.1 are optical tweezers, magnetic tweezers and atomic force microscopy (AFM). The force spectroscopy measurements are done as one end of the molecule is attached to a surface and the other, free end is attached to a probe- an optically trapped bead, magnetic bead or an AFM tip.

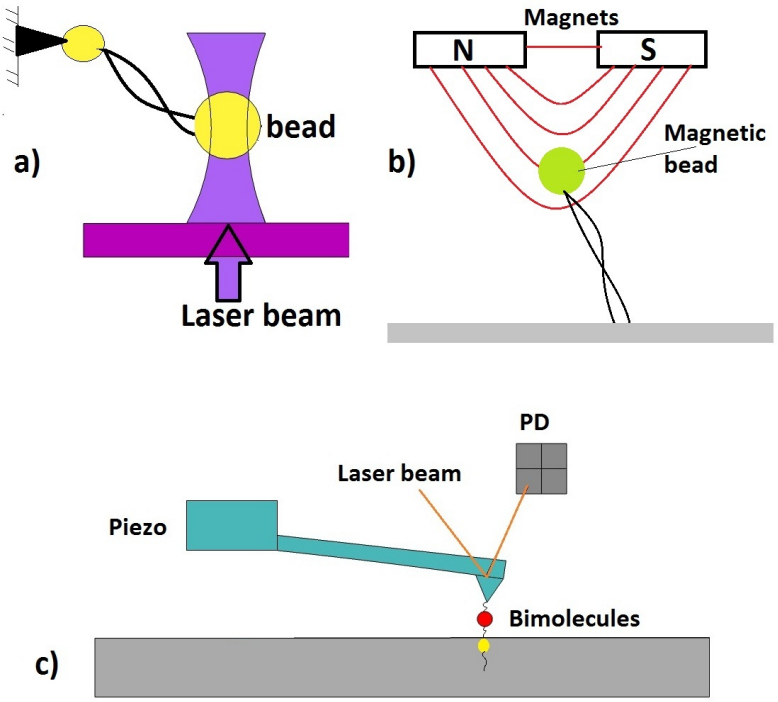


Figure 1.1. The most commonly used single-molecule force spectroscopy techniques. Schematics of (a) optical tweezers, (b) magnetic tweezers and (c) AFM biomolecular force spectroscopy.

Optical tweezers are known as optical traps and manipulate the dielectric beads by small forces with the use of highly focused laser beam from a microscope objective. They are used to trap viruses and bacteria [1], DNA [2,3], living cells [4] and organelles [5] to study their properties in biology. Optical tweezers with their capabilities and drawbacks are well summarized in Neuman's review article [6]. Optical traps hold and

drive the bead against a stable target bead. Optical tweezers can be used to apply forces of 0.1-100 pN on particles in size of nanometers to micrometers and simultaneously to detect the 3D displacement of the trapped particle with sub-nanometer accuracy. Even the optical tweezers is a versatile technique, the limitations should also be considered. The trap's stiffness is dependent on the gradient of the optical field, so due to problems with the intensity the performance of the optical tweezers will degrade. Therefore, high performance optical tweezers depends on the optically homogeneous preparations and purified samples. One of the other limitations is that optical tweezers do not have selectivity. Near the focus of the trapping laser, any dielectric particle can be trapped simultaneously that in order to prevent it the concentration of the particles must be kept at low concentrations. Another important limitation is the local heating that it results from the high intensity at the focus of the trapping laser that forms the optical trap. Local heating causes the viscosity of the medium and the enzymatic activity to change.

In magnetic tweezers the bead is not trapped by the laser beam but the magnets. The super-paramagnetic bead of the tweezers is used as a probe and manipulated by the magnetic field that is generated by permanent magnets or electromagnets [7,8]. Distance of the permanent magnets to the bead is adjusted to change the force as in the electromagnets the current is adjusted to generate different forces [9]. The advantage of magnetic tweezers on the other two is that a sub-piconewton range of forces become accessible and they do not suffer from the local heating as optical tweezers. Despite these advantages permanent magnet configuration lacks manipulation ability of the magnetic particles in three dimensions and magnetic tweezers are not as versatile as optical tweezers or AFM [6].

In the most commonly used single-molecule force spectroscopy techniques AFM is the simplest one in terms of operation. AFM was invented to overcome to the limitations of the scanning tunneling microscope (STM) in imaging mode. However, today AFM is a widely used instrument for nanoscale measurements including the study of surface topography and biomolecular forces. The inter- and intramolecular interaction forces with pico-Newton resolution can be measured by AFM.

In the imaging mode of the AFM, 3D image of the sample surface is produced with the scanning of the cantilever tip on the sample surface [10]. In the force spectroscopy experiments with AFM, cantilever tip is moved towards the sample with vertical motion controlled by a piezoelectric actuator and pressed on the sample. As the tip is retracted from the sample, attachment of the biomolecule tethers the tip to the surface and causes the cantilever to bend toward the surface. The bending of the cantilever (detected by the reflected laser light from the cantilever tip to the photodiode) that has known spring constant determines the value of the force. By new developments, it became possible to combine the AFM imaging with force-spectroscopy. The advantage is that surface topology can be imaged at high resolution that the biomolecules' location can be identified; as a result unbinding forces or force spectrum of the removal can be measured.

Besides the advantages of AFM, it is not easy to specify the interactions of the AFM tip with the molecule of interest in many pulling experiments. The interactions can be nonspecific or contact with the molecule of interest can be inappropriate [6]. With the drawbacks of AFM, long time scale experiment (physiological rate) with force-spectroscopy is also problematic. As AFM cantilever is usually a bimaterial structure and sensitive to temperature gradient, ambient temperature stability becomes the main concern, e.g. thermal expansion with 1 K temperature gradient is approximately 300 nm/K for Bruker's MLCT-C type AFM cantilever. Stiffness of MLCT-C is 0.01 N/m that with the thermal expansion it corresponds to 30 pN force where the measured forces of biomolecules in AFM are 1 pN- 500 pN. As result of the thermal drift in AFM cantilever a time-varying tip-surface distance will occur and may cause the biomolecules to crush by pushing hard, causes to get false force readings and zero-force level to shift [11].

To compensate for the thermal drift in AFM, several methods have been developed; including Kalman filtering [12] for the imaging purposes and local scan method [13] for the AFM based nanomanipulations. Reduction in thermal drift was reported by Wenzler et al. by removing the bimaterial cantilever's metal layer over the base of the cantilever [14]. However, at the end of the cantilevers metal is still used that can-

tilevers are still exposed to thermal deflection. Beyder et al. on the other hand did not modify the existing asymmetric cantilevers but designed and fabricated symmetrically supported torsion levels to reduce probe dependent thermal drift [15]. Without modifying the cantilevers, Fan et al. developed a new method to minimize tip-surface drift by cantilever quality factor ($Q$) feedback [16]. The possibility of athermalization for force spectroscopy in AFM applications without any feedback correction was reported by coupling the AFM cantilevers with thermomechanically matched microstructures [17].

In this thesis, the thermal drift that caused by bimaterial cantilevers' deflection due to ambient temperature change is analyzed analytically, experimentally and with Finite Element Model (FEM). With the results from the analysis various micro-stages that are thermomechanically matched with cantilevers are designed to compensate the thermal drift. Thermomechanically matched micro-stages thermally deflect identically with the cantilevers by the ambient temperature gradients and have same dynamic operations in fluid. Schematic of our method to compensate the thermal drift on AFM cantilevers with thermomechanically matched micro-stage is shown in Figure1.2.

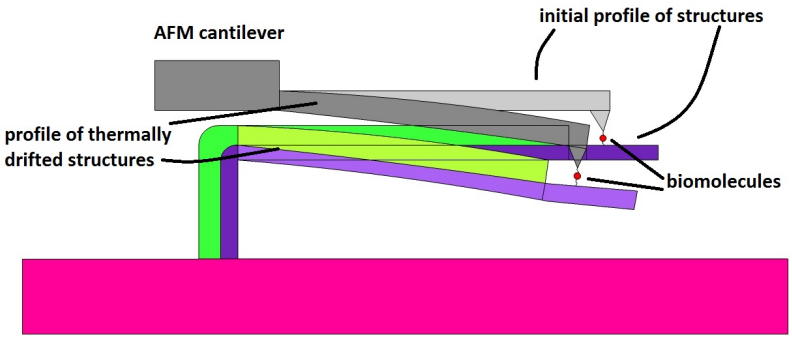


Figure 1.2. Schematic of our method for athermalization of AFM cantilevers in a biomolecular experiment.

With the designed micro-stages constant tip-to- membrane distance under thermal gradient is provided as piezoactuator keeps the distance between the cantilever and substrate the same. Indeed, the resulted constant peak force exerted on the

biomolecules prevents the biomolecules to crush. The other problem of thermal drift in cantilevers, shift in zero-force level with the cantilever bending can be corrected by reading the micro-stage's deflection. Lastly, in order to be sure that micro-stages' deflection is due to the thermal drift not the biomolecular interaction forces, the micro-stages should be much stiffer than the cantilevers.

# 2. THERMOMECHANICAL MODEL OF AN AFM CANTILEVER

The design effort for micro-stages is focused on

- Thermal deflection: Due to the ambient temperature changes cantilever deflects and causes false force readings, shift in zero-force level and biomolecules that stand on the sample stage to crush with the cantilever tip. Steady state thermal deflections of the cantilevers are analyzed and the aim is to have same deflection/K values for the cantilever and the MEMS for various reasons.

- Dynamic operation: Micro-stages are designed to have the same dynamic operation (transient state temperature distribution) with the cantilevers.

- Stiffness: The designed micro-stages are designed as alternative sample stages in AFM. Even with the new sample stages cantilever still bends and causes zero-force level to shift. Zero-force level shift can be corrected by the micro-stage's membrane displacement and the membrane displacement must be due to the thermal drift not the biomolecular interaction forces. To make sure that membrane displacement is due to the thermal drift, the micro-stages should be much stiffer that the cantilevers.

In order to design the micro-stages with the design criteria firstly analytical formulations are used to analyze cantilevers' behavior in heat transfer then verified FEM simulation results in COMSOL Multiphysics 3.5. Analytical modeling is a good design tool and used for optimization in order not to consume too much time during FEM simulations. FEM also has some advantages over analytical modeling; it handles complex geometries well and secondary effects can also be analyzed.

### 2.1. Thermal Deflection

The deflection of the cantilever is proportional to the mismatch of the coefficient of thermal expansions of the cantilever layers. In our experiments, we used a 310 $\mu$m long, 20 $\mu$m wide, triangular-shaped bimaterial cantilever (MLCT-C, Bruker Probes) that is made of silicon nitride ($SiN_x$) and gold (Au). In our calculations, the triangular shaped cantilever is modeled as a rectangular cantilever and the cantilever tip deflection is calculated to be 339 nm/K with the analytical deflection model

$$\phi = \frac{E_1}{E_2} \tag{2.1}$$

$$n = \frac{h_1}{h_2} \tag{2.2}$$

$$K = 4 + 6n + 4n^2 + \phi.n^3 + (\frac{1}{\phi.n}) \tag{2.3}$$

$$(\frac{1}{R}) = 6(\alpha_1 - \alpha_2)[\frac{h_1 + h_2}{{h_2}^2.K}]\Delta T \tag{2.4}$$

$$x = (\frac{1}{2R})L^2 \tag{2.5}$$

where $E_1$ is the Young's modulus of cantilever's first layer and $E_2$ is the Young's modulus of cantilever's second layer, $\phi$ is Young's modulus ratio, $h_1$ is thickness of cantilever's first layer, $h_2$ is thickness of cantilever's second layer, $n$ is the thickness ratio of the cantilever layers, $K$ is a coefficient, $1/R$ is cantilever's radius of curvature, $\alpha_1$ is coefficient of thermal expansions of the cantilever's first layer, $\alpha_2$ is coefficient of thermal expansions of the cantilever's second layer, $L$ is the length of the cantilever, $\Delta T$ is the ambient temperature change and $x$ is the deflection of the cantilever tip [18].

Material properties of $SiN_x$ and Au with thickness in MLCT-C type cantilever are shown in Table 2.1 below.

Table 2.1. Material properties of $SiN_x$ and Au with thickness in MLCT-C type cantilever.

| | **$SiN_x$** | **Au** |
|---|---|---|
| $E$ | 14x$10^{10}$ N/$m^2$ | 8x$10^{10}$ N/$m^2$ |
| **CTE ($\alpha$)** | 0.8x$10^{-6}$ m/m.K | 8.6x$10^{-6}$ m/m.K |
| **Thickness ($h$)** | 550 nm | 45 nm |
| $k_{cond}$ | 18.5 W/m.K | 21.9 W/m.K |

With the same analytical model MLCT-D and MLCT-B's tip deflections are also calculated as 178 nm/K and 155 nm/K,respectively. Other than analytical calculations, also with 2D FEM simulations (by adding the effect of thermal expansion to the structural mechanics module) cantilever beams are modeled for the deflection analysis. As the cantilevers in AFM are usually mounted at an angle relative to the X,Y plane, which is typically around 15 degrees, cantilevers in the simulations are modeled as 15° tilted. One end fixed cantilever beam, MLCT-C, with 1 K change in temperature deflected 337.2 nm/K as shown in Figure 2.1. With the same deflection profiles, that are shown in Figure A.1 and A.2, MLCT-D which is 225 $\mu$m long, 20 $\mu$m wide deflected 177.69 nm/K and MLCT-B which is 210 $\mu$m long and 20 $\mu$m wide deflected 154.58 nm/K.

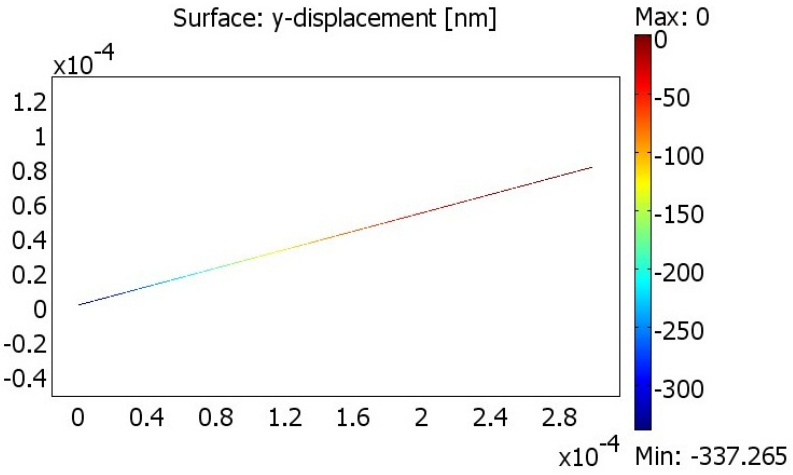


Figure 2.1. 2D FEM simulation for the deflection analysis of MLCT-C type cantilever.

## 2.2. Heat Transfer

Transition of thermal energy due to spatial temperature difference is heat transfer and it is classified into various modes; conduction, convection and radiation. Conduction, also called diffusion, refers to the heat transfer across the medium from the more energetic to the less energetic particles of a substance by molecular activity. The other mode, convection, refers to the heat transfer between a surface and a moving fluid. It is due to energy transport not only by the random motion of molecules but also by the bulk motion of the fluid. The third mode of heat transfer, radiation, refers to the heat transfer by emission of energy by matters in the form of electromagnetic waves and thermal radiation propagates in the absence of an intervening medium, most efficiently in vacuum [19].

For complete cancelation of the thermal drift, not only the same thermal deflection of cantilever and micro-stage is required but also the same time constants. Time constants could be found with the help of the lumped system analysis (lumped capacitance model) for thermal systems. Cantilever was modeled as n number of segments of thermal resistances with the lumped system analysis which is shown in Figure 2.2. Computational domain is in oblique shape to prevent the spatial variation imposed by the top boundary on the AFM cantilever. The bottom boundary models the sample

stage for some simulations and the angle between the bottom boundary and the cantilever is kept at 15 degrees. Top and bottom of the fluid boundaries are taken fixed at 0°C. The initial temperature of the cantilever tip is also taken 0°C. The reason for different up and down resistances is because of the different distances from the cantilever surface to the fluid boundaries (top and bottom). As the distance between the cantilever's top surface to the top outer boundary of fluid is taken 100 $\mu$m (drop of fluid size is taken into account), the distance between the cantilever tip to the bottom outer boundary is starting from 0.1 $\mu$m (distance between sample stage and cantilever tip is taken into account) and increasing with an angle of 15 until the end of the cantilever as the cantilevers in AFM are usually mounted at an angle which is typically around 15 degrees (explained in the thermal deflection section above). The model is working by increasing the temperature of cantilever tip to a known temperature with an unknown temperature that is given to the cantilever base. Temperature of the model is modeled as a voltage source.

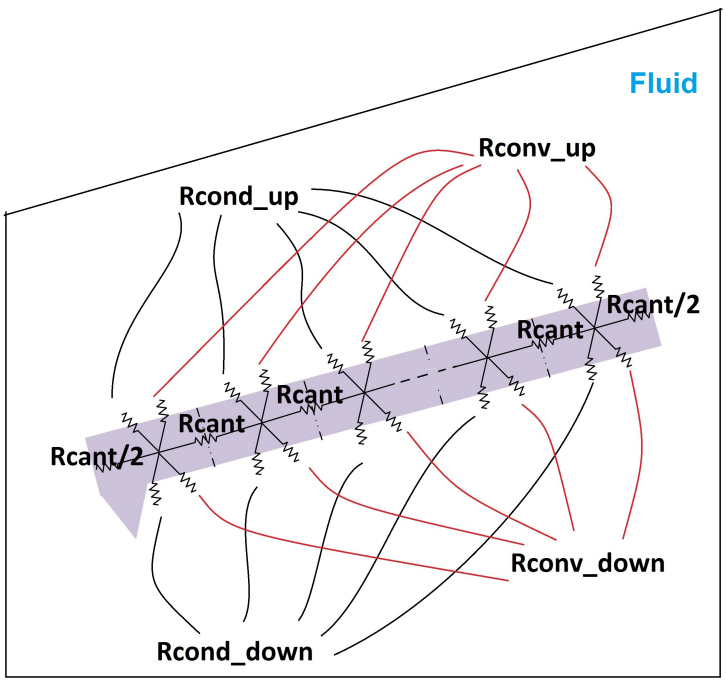


Figure 2.2. Lumped model of the cantilever in fluid.

In the model, heat is transferred on the cantilever by conduction, between cantilever and fluid by both conduction and convection.

$R_{cond}$, thermal resistance for conduction, is calculated as follows

$$R_{cond} = \frac{L}{kA} \tag{2.6}$$

where $L$ is the length of the cantilever, $k$ is the thermal conductivity and $A$ is the cross sectional area of the cantilever. $R_{cant}$ is also a thermal resistance for conduction that it is also calculated by Equation 2.6. $R_{conv}$, thermal resistance for convection, is calculated as follows

$$R_{conv} = \frac{1}{hA} \tag{2.7}$$

where $h$ is convective heat transfer coefficient and taken as 40 W/m$^2$K for air, $A$ is the overall surface area of the cantilever. Equivalent thermal resistance of the lumped capacitance model is calculated through $R_{cond}$, $R_{conv}$ and $R_{cant}$ in order to find the time constant (dynamic operation) of the cantilever tip and the time constant of the cantilever tip in fluid is calculated with the equations below where $c$ is the heat capacity of cantilever's layers, $C_{eq}$ is the equivalent capacitance of the system, $m$ is the mass of the cantilever, $\rho$ is the density of the cantilever, $V$ is the volume of the cantilever, $\tau$ is the time constant of the cantilever tip, $R_{eq}$ is the equivalent thermal resistance of the system that is calculated with the lumped system analysis and $t_{rise}$ is the rise time of the cantilever's tip. Material properties of air and water is shown in Table 2.2.

$$c = \frac{C_{eq}}{m} = \frac{C_{eq}}{\rho V} \tag{2.8}$$

$$\tau = R_{eq}C_{eq} = R_{eq}\rho V c \tag{2.9}$$

Table 2.2. Material properties of Air and Water.

| | **Air** | **Water** |
|---|---|---|
| $c$ | 1158 J/kg.K | 4181.3 J/kg.K |
| $\rho$ | 1.225 kg/m$^3$ | 997 kg/m$^3$ |
| $k_{cond}$ | 26.3x10$^{-3}$ W/m.K | 0.6 W/m.K |
| $h$ | 18.5 W/m.K | 21.9 W/m.K |

With FEM analysis results, from the temperature vs. time graphs of the cantilever tips, calculation of the rise time is possible that to compare the results the analytically calculated time constants should be turned into rise time. For a simple one stage low pass RC network, rise time is proportional to the network time constant. In case of the RC network, the 10% level is reached after 0.105 time constants and the 90% after 2.302 time constants; thus the rise time is (2.302 – 0.105) time constants which is 2.197 time constants or $2.197\tau$ as shown in the equation below.

$$t_{rise} = 2.197\tau \tag{2.10}$$

By the lumped model MLCT-C type cantilever the rise time in air on the tip is calculated as 7 ms with the analytical model. Calculated equivalent resistances for rise time, in air and water, with the lumped model for MLCT-C type cantilever are shown in the Table 2.3 and Table 2.4 below.

Table 2.3. Calculated equivalent thermal resistances with the lumped model for rise time of MLCT-C type cantilever in air.

| **Rcond**$_{up}$ | **Rconv**$_{up}$ | **Rcond**$_{cant}$ |
|---|---|---|
| 6.13x10$^5$ $K/W$ | 4.03x10$^6$ $K/W$ | 6.33x10$^5$ $K/W$ |

Table 2.4. Calculated equivalent thermal resistances with the lumped model for rise time of MLCT-C type cantilever in water.

| $\mathbf{Rcond}_{up}$ | $\mathbf{Rconv}_{up}$ | $\mathbf{Rcond}_{cant}$ |
|---|---|---|
| 2.68x$10^4$ $K/W$ | 3.22x$10^5$ $K/W$ | 6.33x$10^5$ $K/W$ |

In both fluids $\text{Rcond}_{up}$ is smaller than $\text{Rcond}_{cant}$ so it is the dominant resistance in the rise time calculations of cantilever. As $\text{Rcond}_{up}$ depends on the surface area of the cantilever, in order to match the thermal time constants of micro-stages with cantilevers, micro-stage area is decided to be chosen approximately same as the cantilever surface area.

To verify the rise time result of the analytical modeling by the lumped model, 2D FEM simulation (general heat transfer module) of MLCT-C type cantilever's heat transfer in air is done. The computational domain is taken asymmetric to have the same boundary distances (between the cantilever and fluid boundary) with the lumped model. Boundary conditions of the model are shown in the Figure 2.3a. There is no flow in fluid and by giving heat flux of 50x$10^4$ W/m$^2$ to the tip boundary rise time is given as 8 ms as shown in the Figures 2.3b and 2.4 below. It was calculated as 7 ms in the analytical model that this result (8 ms) verifies the analytical result.

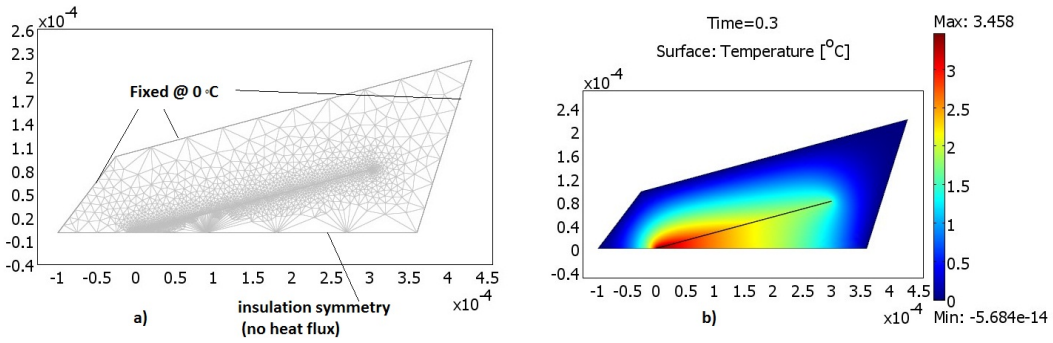


Figure 2.3. 2D FEM for MLCT-C type cantilever meshed geometry (a) and 2D FEM for MLCT-C type cantilever's rise time (b).

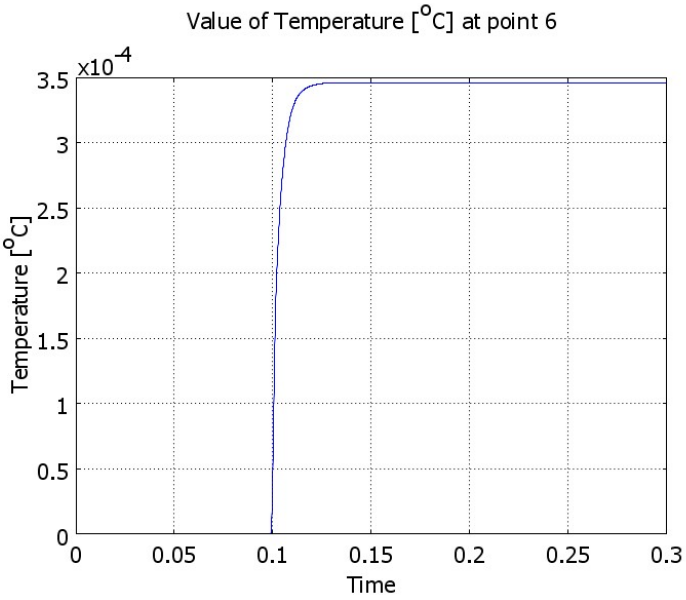


Figure 2.4. 2D FEM simulation result for MLCT-C type cantilever's rise time on tip in air.

By giving heat flux of 50x10$^4$ W/m$^2$ to the tip boundary of the MLCT-C type cantilever in water the rise time on the tip is given as 30 ms with the 2D FEM simulation, as shown in the Figures 2.5 and 2.6 below.

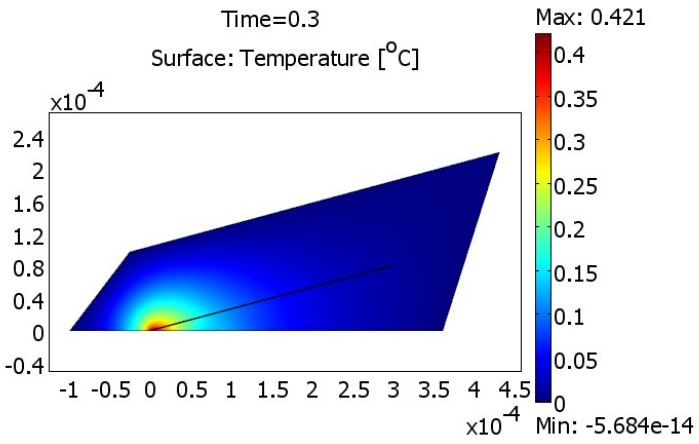


Figure 2.5. 2D FEM for MLCT-C type cantilever's rise time on tip in water.

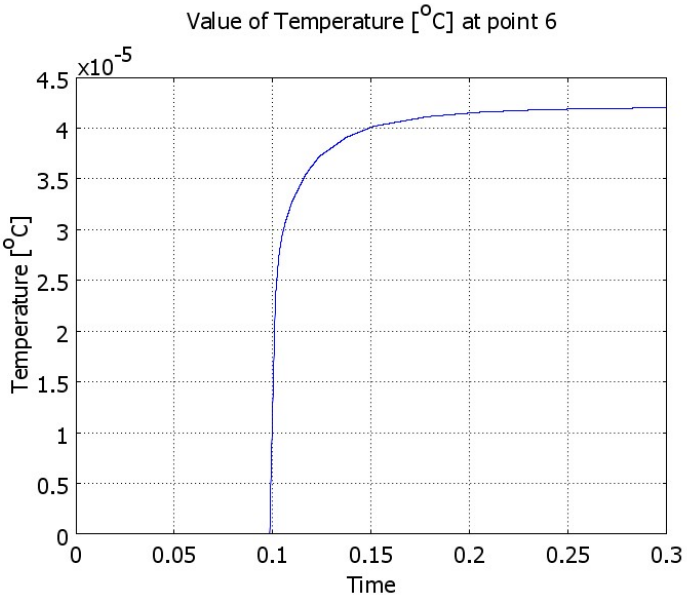


Figure 2.6. 2D FEM simulation result for MLCT-C type cantilever's rise time on tip in water.

By improving the 2D FEM of cantilever's heat transfer in fluid the cantilever is also modeled as staying on top of a Ti micro-stage with an angle of 15 (the reason for the angle is explained in 2D FEM for MLCT-C type cantilever's thermal deflection simulation, Figure 2.1). As the designed micro-stages are made of Ti/Al and the top surface is Ti, in this improved model micro-stage is chosen Ti. The inclined line between the cantilever chip and the Ti micro-stage is drawn to dissolve the meshing problem of FEM, complex meshed model is shown in Figure 2.7a. Cantilever/the micro-stage interaction and the chip of the cantilever was not considered in the analytical model and the 2D FEM simulation for MLCT-C type cantilever's rise time in fluid. With the complex model, by giving heat flux of 50x10$^4$ W/m$^2$ to the MLCT-C type cantilever tip, the rise time on the tip in air is given as 1.8 ms, as shown in the Figures 2.7b and 2.8 below. In 2D FEM simulation, outer boundaries are fixed at 0°C when the boundary on the Ti micro-stage is determined as insulation symmetry (no heat flux).

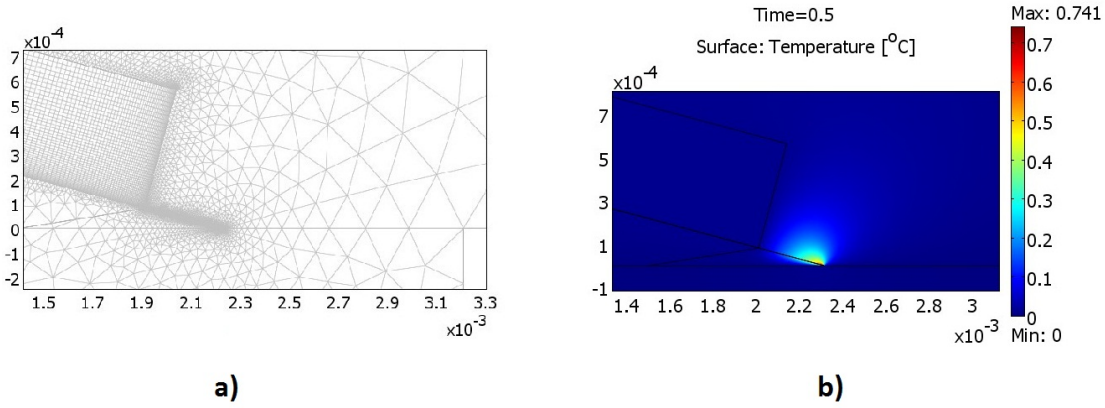


Figure 2.7. Complex 2D FEM for MLCT-C type cantilever meshed geometry (a), Complex 2D FEM for MLCT-C type cantilever's rise time in air (b).

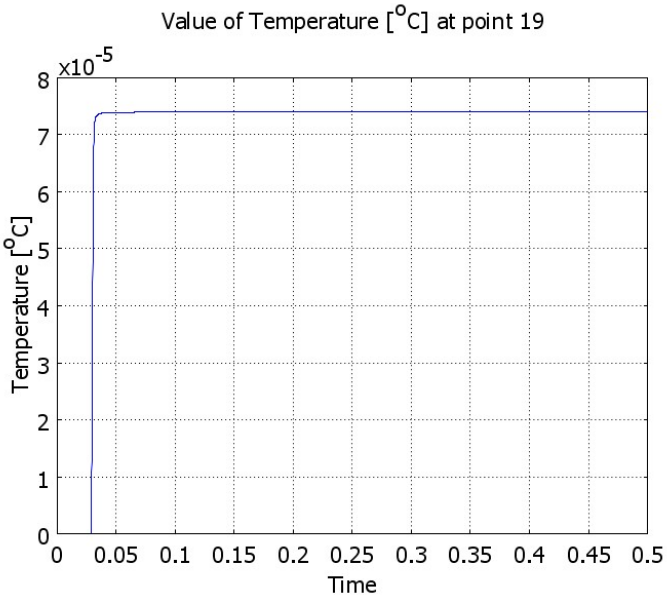


Figure 2.8. Complex 2D FEM simulation result for MLCT-C type cantilever's rise time on tip in air.

With the same boundary conditions and same heat flux the complex 2D FEM for the rise time simulation of MLCT-C type cantilever tip and the graph of temperature vs. time of the cantilever's tip in water are shown in the Figures 2.9 and 2.10. From the graph, the rise time is calculated as 15 ms.

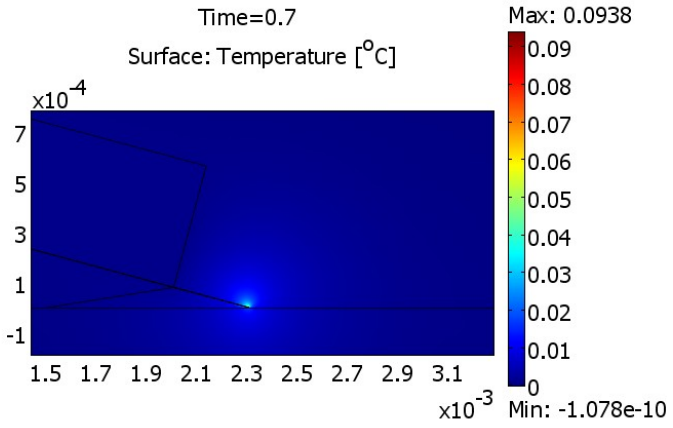


Figure 2.9. Complex 2D FEM for MLCT-C type cantilever's rise time in water.

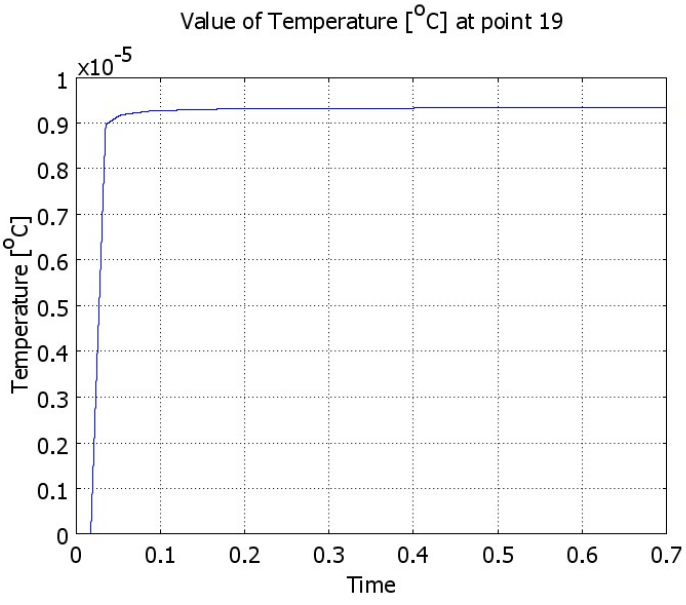


Figure 2.10. Complex 2D FEM simulation result for MLCT-C type cantilever's rise time on tip in water.

Rise time of cantilever tip in air decreased from 8 ms to 1.8 ms when rise time of cantilever in water decreased from 30 ms to 15 ms with the new complex model as shown in Figure 2.7 and Figure 2.9, respectively. The reason of the drop in rise times is the high thermal conductivity of Ti micro-stage. If the membrane material is chosen as a different material like Parylene-C, higher rise times than Ti micro-stage case is expected because of low thermal conductivity of Parylene-C. Material properties of Ti, Al, Si and Parylene-C is shown in Table 2.5. Indeed, for the future work, different sample-stages with different materials like Parylene-C can be designed.

Table 2.5. Material properties of Ti, Al, Si and Parylene-C.

| | **Ti** | **Al** | **Si** | **Parylene-C** |
|---|---|---|---|---|
| $k_{cond}$ | 21.9 W/m.K | 237 W/m.K | 149 W/m.K | 0.0837 W/m.K |
| $c$ | 523 J/kg.K | 900 J/kg.K | 700 J/kg.K | 170 J/kg.K |
| $\rho$ | 4506 kg/m$^3$ | 2692 kg/m$^3$ | 2420 kg/m$^3$ | 1289 kg/m$^3$ |

- Heat capacity of water is larger than heat capacity of air that for a larger heat capacity there should be a smaller temperature change if the heat losses are assumed similar [20]. The one order of magnitude difference between rise times in air and water is likely to be explained by their capacity differences.

- From the lumped model, the most dominant resistance is calculated as $R_{cond}$ which is between the cantilever and fluid, is shown in Table 2.3 and Table 2.4. As a result of this for the rise time calculations it is understood that surface area is the most efficient factor in dynamic operation. While designing the micro-stages, surface area of the cantilever is used approximately as same as the micro-stages' surface area in order to have the same dynamic operations.

# 3. EXPERIMENTAL SETUP AND CHARACTERIZATION

Motivation of building an experimental setup is to validate the results of the analytical modeling. To validate the thermal deflection of the MLCT-C type cantilever in air, optical characterization setup that consists of cantilever, laser ($\lambda$ = 532 nm, 2.5 mW max), lens system, thermoelectric cooler (TEC), semiconductor temperature sensor (LM35), power meter (Thorlabs Instrumentation, Optical Power Meter, PM100A), photodiode (Thorlabs Instrumentation, S120VC), power source and oscilloscope is used. The cantilever was mounted on TEC (7103), the temperature gradient was controlled with the temperature sensor and by the optics the reflected laser light from cantilever's tip to the photodiode (by knife-edge technique) was read by the power meter. Optical setup that is used for detection of cantilever's deflection is shown in the Figure 3.1 below.

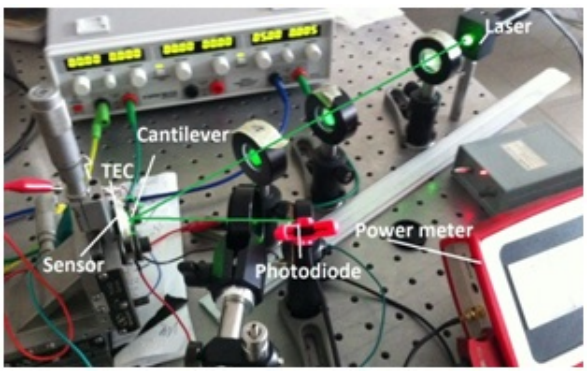


Figure 3.1. Optical setup that is used to detect cantilever's deflection.

The optical readout system in the optical setup schematics is shown in the Figure 3.2 below. The optics is aligned to focus the laser on the cantilever with a spot size of 15 $\mu$m.

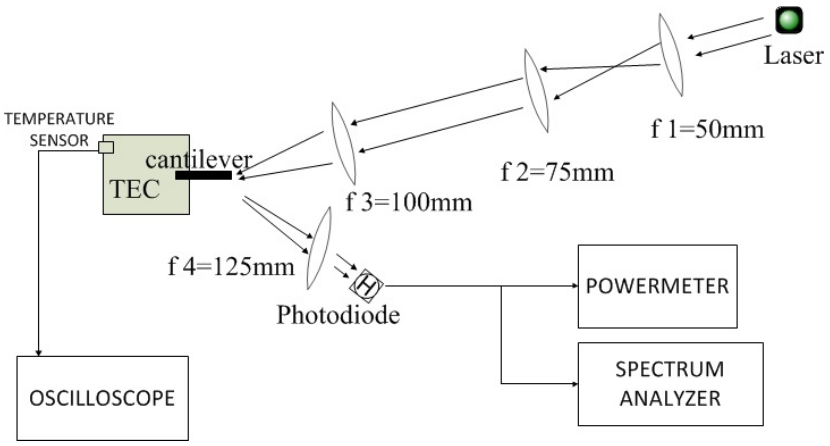


Figure 3.2. Optical setup in schematics.

The knife-edge technique to read the reflected laser light is shown in the Figure 3.3 below. By the cantilever's displacement due to the temperature change causes the laser spot to move on the photodiode/detector. Movement of the laser spot results the power on the power meter to change so the displacement of the cantilever will be measured.

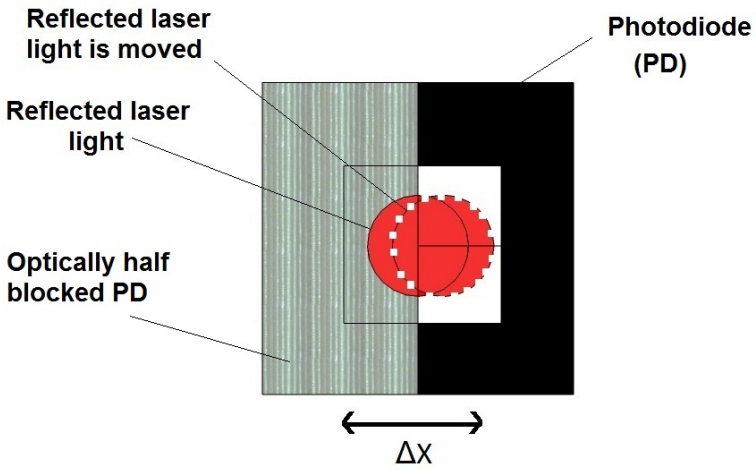


Figure 3.3. The knife-edge technique.

A micromanipulator was brought in contact with the tip of the cantilever. The cantilever was displaced using the manipulator and the displacement was measured

using the manipulator with nanometer sensitivity that is calculated as 0.31 V/$\mu$m or 3.22 $\mu$m/V. The graph that shows the sensor output versus displacement of the tilted cantilever's tip to find the sensitivity from its slope is shown in the Figure 3.4 below.

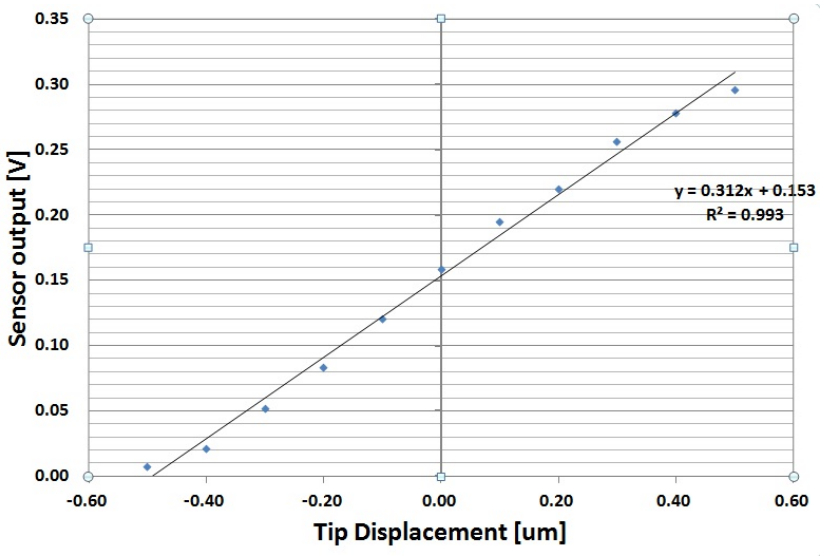


Figure 3.4. Sensitivity of the sensor (Displacement calibration graph).

By cooling the TEC with reverse current, temperature gradient on the temperature sensor is recorded with the oscilloscope; and with the sensitivity of the setup, corresponding displacement on the cantilever's tip is calculated from the photodiode's voltage. As Figure 3.5 shows, temperature of the system decreases from 25.2°C to 22°C. The semiconductor-based temperature sensor used in this setup, LM35, has readout accuracy within the experimental range as 0.5 K. Figure 3.6 shows the corresponding displacement of the cantilever measured by photodiode and the measurement accuracy of the power meter is +/- 0.5x10$^{-3}$ V for 1 V rated voltage range. The accuracy of the power meter corresponds to 16.1 nm accuracy in the measurements. From the graphs that are shown in Figure 3.5 and Figure 3.6 below, deflection of the cantilever's tip in air is calculated as 288.4 nm/K. This experimental result is acceptable as compared with the analytical deflection of MLCT-C type cantilever's tip which was calculated as 339 nm/K and the 2D FEM simulation of thermal deflection model which was 337.2 nm/K.

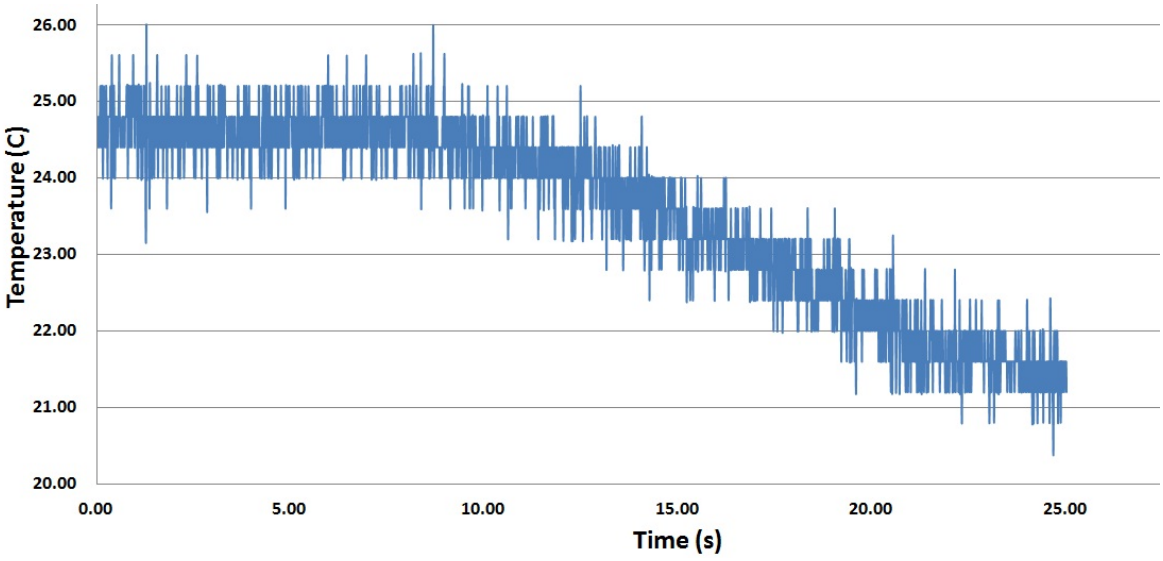


Figure 3.5. Graph of temperature of the sensor versus time as TEC is cooled.

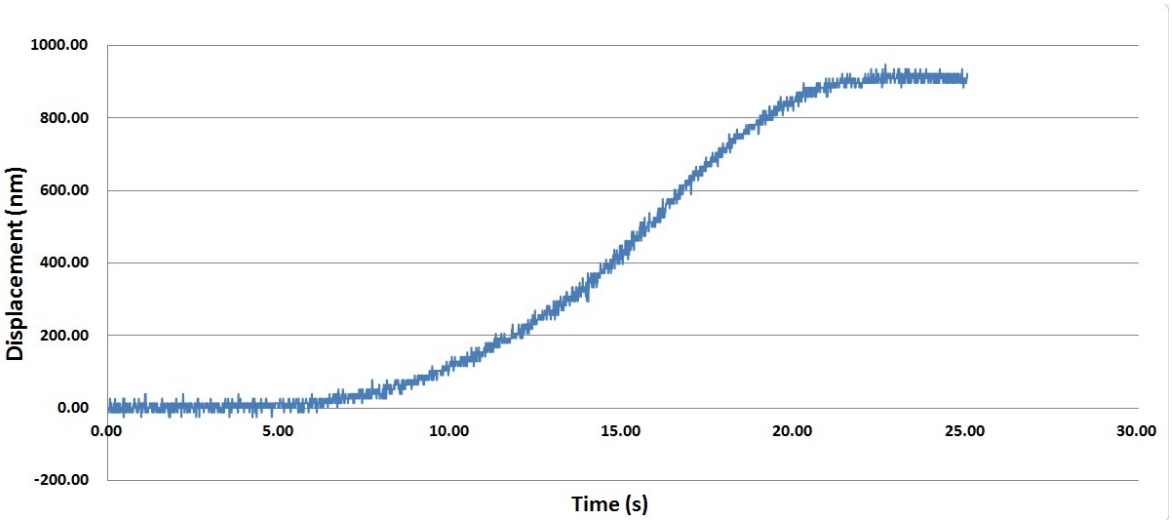


Figure 3.6. Graph of tip of cantilever's displacement versus time as TEC is cooled.

To find the possible minimum detectable displacement of the experimental setup, noise spectrum of the optical setup is found with the spectrum analyzer (HP4195). Noise data that detected from the photodiode when the laser spot is at the middle of the photodiode (with 470 $\mu$W optical power) is shown in the Figure 3.7 below. Minimum detectable displacement in 1 Hz band is calculated with the noise data and the sensitivity as 0.2 nm.

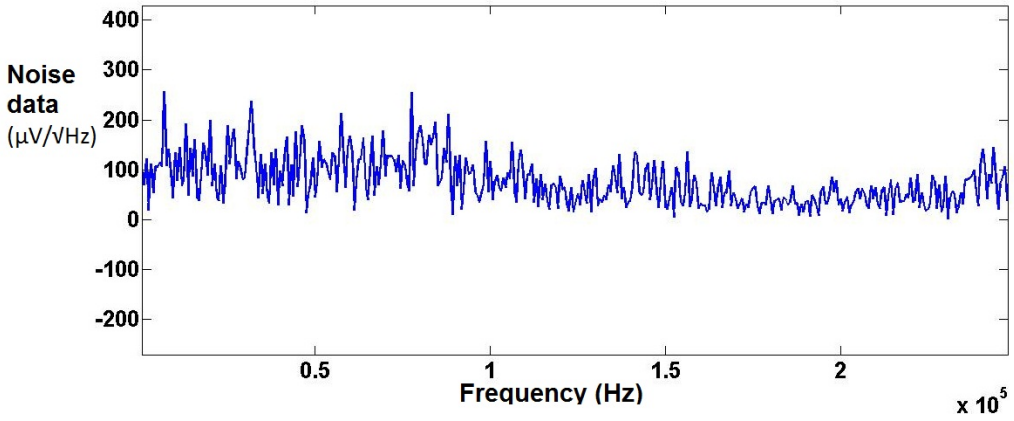


Figure 3.7. Noise spectrum of the setup.

Dynamic time constant of the cantilever is tried to be measured by heating the cantilever by the TEC. Time constant of the system is found as 110 s that cantilever's time constant which is in the order of 10 ms is not possible to detect. Time constant of the system is limited by TEC, a different optical setup to detect the cantilever's time constant should be used in the future works.

# 4. DESIGN OF COMPENSATING MICRO-STAGES

Based on the analytical and 2D FEM data obtained by using the cantilever models, ideal micro-stages for these particular cantilevers are designed by considering the thermal deflection, dynamic operation and stiffness. Materials for the micro-stages are chosen as titanium (Ti) and aluminum (Al) for the materials' CTE mismatch that results in thermal deflection.

- The layer thicknesses are determined to match the deflection of the particular cantilevers and also stiffness criteria is also been taken into account.

- Micro-stages' membranes deflect by the bimaterial legs. Bimaterial legs' lengths are decided by the bimaterial leg deflection analysis as deflection increases with length of the bimaterial legs. There was a trade-off between the deflection and the stiffness. As the bimaterial legs get longer and micro-stage deflection increases to match with the deflection of the cantilever, stiffness decreases.

- With the analytical heat transfer lumped model it is understood that surface area of the cantilever determines the dynamic operation that in order to match the thermal time constants micro-stage area is designed approximately same as the cantilever surface area. To have approximately the same area with the cantilever, the bimaterial legs needed thinner width and it caused to loose from the stiffness.

Micro-stages are designed to thermomechanically match with the particular cantilevers and verified with FEM. Note that the micro-stages are approximately two orders of magnitude stiffer than the selected cantilevers, and hence the membrane deflection due to biomolecular interactions will still be insignificant.

## 4.1. Various Micro-stage Designs For Cantilevers

Micro-stages consist of 600 nm-thick Ti and 900 nm-thick Al bimaterial legs and 900nm-thick Ti membranes. Decision for the bimaterial thickness is given by adapting the analytical model that was used to find the cantilever deflection to micro-stages. Thickness ratio of the layers is dependent on bimaterial leg deflection as shown in the previous chapter's Equations 2.1-2.5, so the thickness ratio is optimized by the deflection analysis. Material decision of the layers is given with respect to the CTE mismatch of the metals which is shown in Table 4.1 and the metals' sputtering possibility in cleanroom. Stiffness of the micro-stages is also another criteria in the decision of the thicknesses. As thicker bimaterial leg increases stiffness, there is also a thickness limitation for the fabrication process.

Table 4.1. Coefficient of Thermal Expansion (CTE) of Al and Ti.

| | **Al** | **Ti** |
|---|---|---|
| **CTE** | 25x10$^{-6}$ m/m.K | 8.6x10$^{-6}$ m/m.K |

For MLCT-C type cantilever five various micro-stages and for MLCT-D type cantilever two various micro-stages are designed. For MLCT-B type cantilever one micro-stage is also designed. Criteria for the designs were to have the same deflections and the dynamic operation with the cantilevers' tips and to be much stiffer than the cantilevers. In this section only one design per three types of cantilevers are given; other designs and their simulation results for thermal deflection, heat transfer and stiffness can be find in the appendix.

### 4.1.1. Dimensions of the micro-stages, schematics

Dimensions of designed one micro-stage for MLCT-C type cantilever are shown in the Figure 4.1 below. Design C1 consists of two 25 $\mu$m x 150 $\mu$m bimaterial legs and a 50 $\mu$m x 100 $\mu$m Ti membrane. 3D illustration of Design C1 is also shown in the Figure 4.2 below.

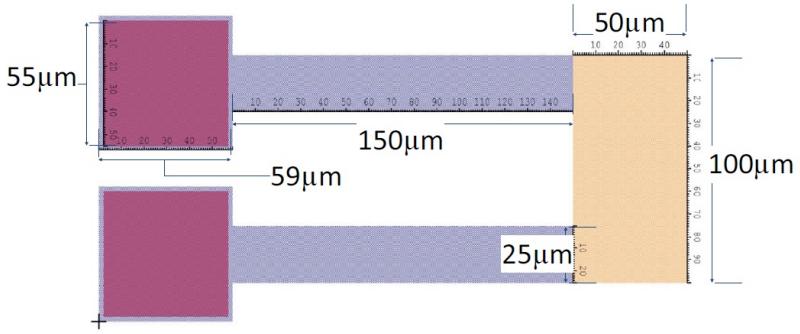


Figure 4.1. Dimensions of Design C1.

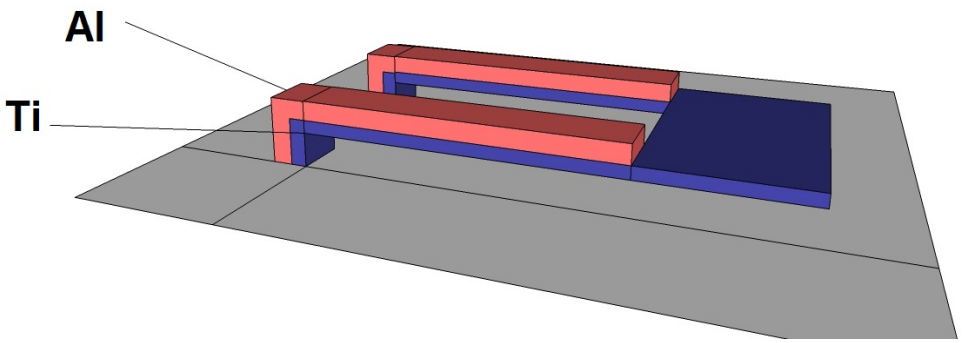


Figure 4.2. 3D illustration of Design C1.

Dimensions of designed one micro-stage for MLCT-D type cantilever are shown in Figure 4.3 below. Design D1 consists of four 25 $\mu$m x 160 $\mu$m bimaterial legs, four 5 $\mu$m x 15 $\mu$m Ti pins and a 100 $\mu$m x 100 $\mu$m Ti membrane.

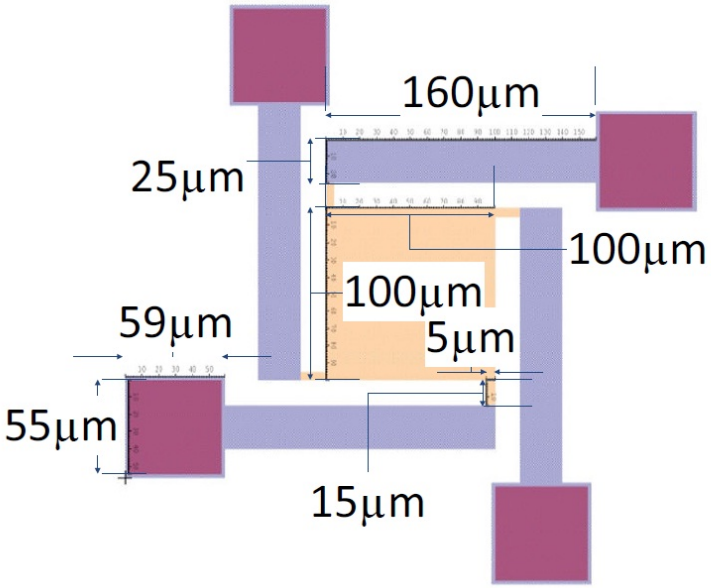


Figure 4.3. Dimensions of Design D1.

Dimensions of the designed micro-stages for MLCT-B type cantilever are shown in Figure 4.4 below. Design B1 consists of four 25 $\mu$m x 150 $\mu$m bimaterial legs, four 5 $\mu$m x 15 $\mu$m Ti pins and a 100 $\mu$m x 100 $\mu$m Ti membrane.

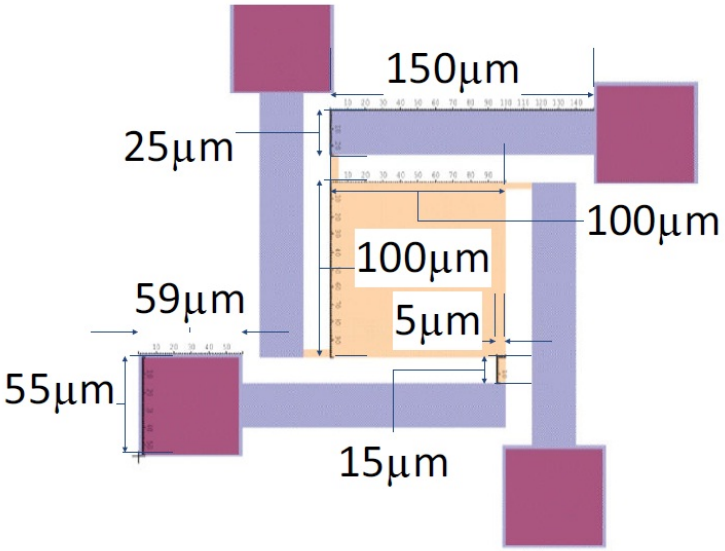


Figure 4.4. Dimensions of Design B1.

### 4.1.2. Thermal Deflection

For the 3D thermal deflection simulations (by adding the effect of thermal expansion to the structural mechanics module) of the micro-stages in FEM, micro-stages are heated up 1°C. Thermal deflection 3D FEM simulation results of Design C1, Design D1 and Design B1 are shown in Figure 4.5, Figure 4.8 and Figure 4.11, respectively. Thermal deflection of Design C1 is 330.2 nm/K at the tip of the structure that shown in Figure 4.5, and at the point shown in Figure 4.7 thermal deflection is 299 nm/K.

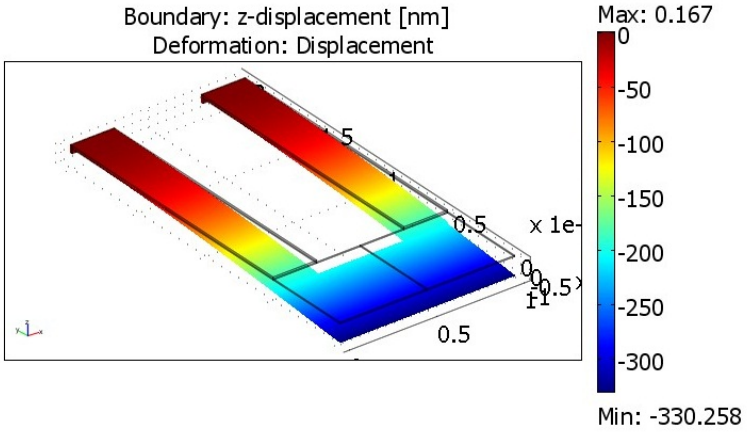


Figure 4.5. 3D Thermal deflection simulation result in FEM for Design C1.

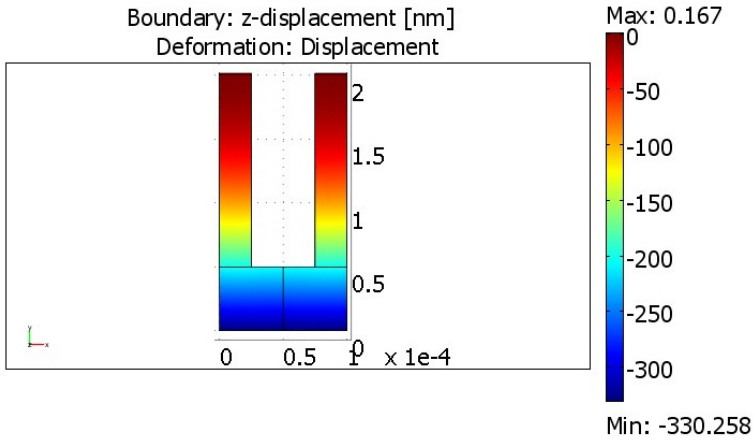


Figure 4.6. 3D Thermal deflection simulation result in FEM for Design C1, top view.

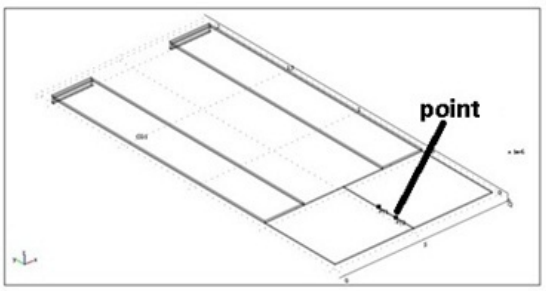


Figure 4.7. Point for 3D thermal deflection simulation result in FEM for Design C1.

Thermal deflection of Design D1 is 170 nm/K at the center of its membrane and the 3D FEM simulation is shown in Figure 4.8.

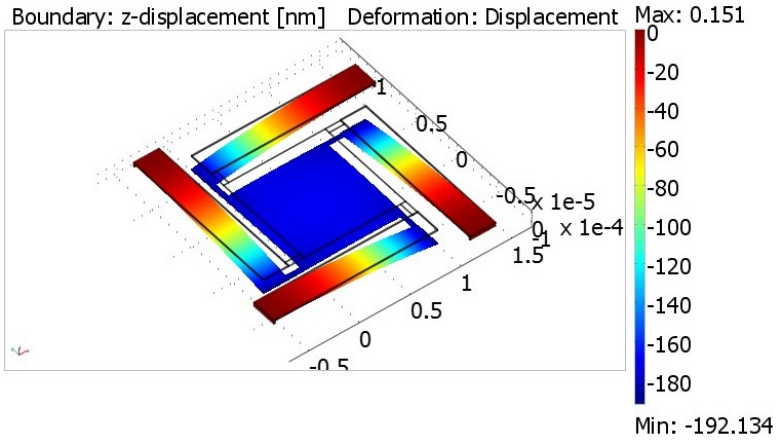


Figure 4.8. 3D Thermal deflection simulation result in FEM for Design D1.

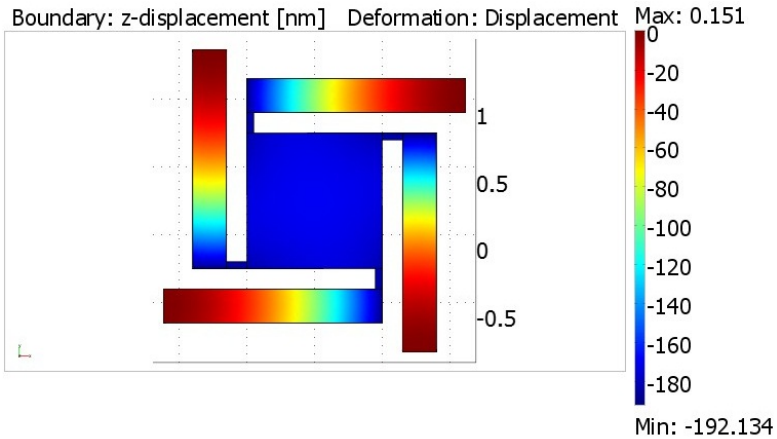


Figure 4.9. 3D Thermal deflection simulation result in FEM for Design D1, top view.

Thermal deflection of Design B1 is 151 nm/K at the center of its membrane and the 3D FEM simulation is shown in Figure 4.10.

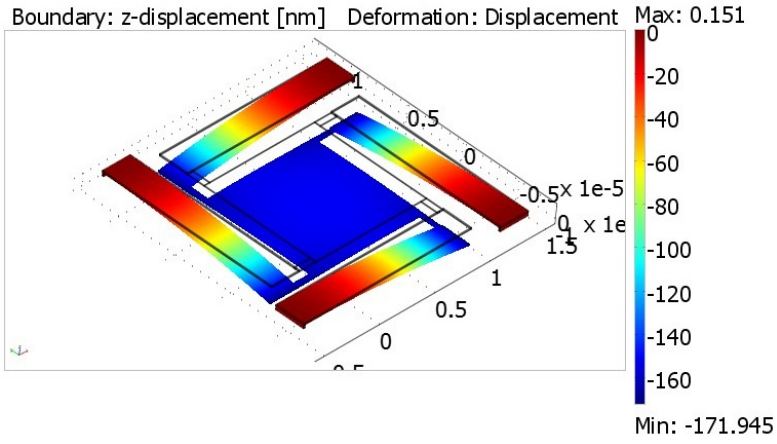


Figure 4.10. 3D Thermal deflection simulation result in FEM for Design B1.

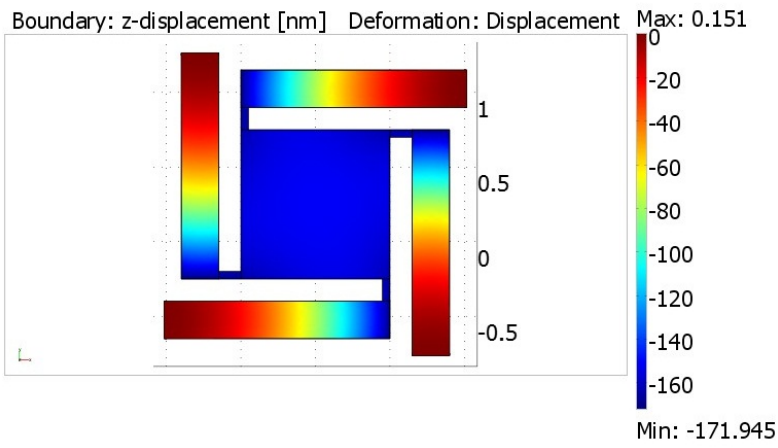


Figure 4.11. 3D Thermal deflection simulation result in FEM for Design B1, top view.

### 4.1.3. Heat Transfer

For the 3D FEM simulation of Design C1's heat transfer, outer boundaries of the fluid and the pads of the legs are fixed at 0°C when the boundary under micro-stage is determined as insulation symmetry (no heat flux). Heat flux of 500 W/m$^2$ is given to the micro-stage from its membrane surface, the rise time in air on the point that is shown in Figure 4.7 is given as 1.7 ms with the simulation. With the same boundary conditions and heat flux, the rise time in water on the same point is given as 85 ms. 3D FEM simulation results for Design C1's the rise times in air and water are shown in Figure 4.12 and Figure 4.13 below. For the MLCT-C type cantilever the rise time in air and water was 8 ms and 30 ms, respectively. Design C1 rise times are in the same order of magnitudes with MLCT-C type cantilever rise times. By coupling of the designs rise times of cantilever and micro-stages will be expected to be similar.

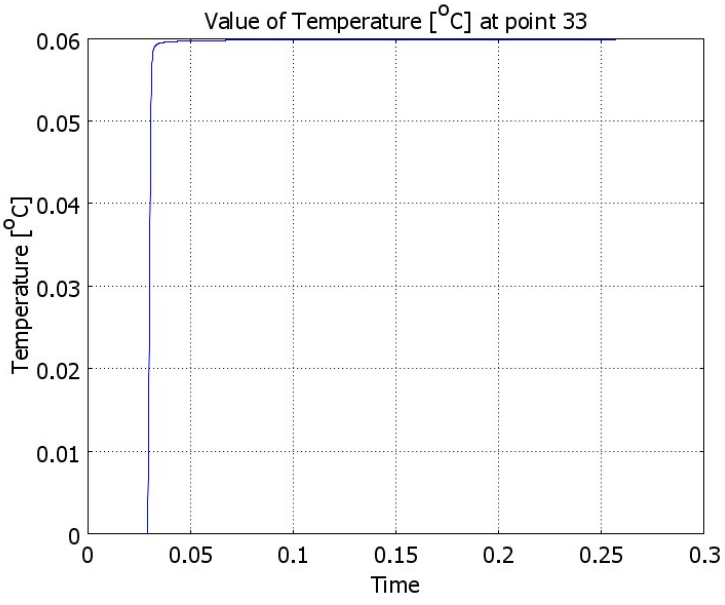


Figure 4.12. 3D FEM simulation result for Design C1's rise time in air.

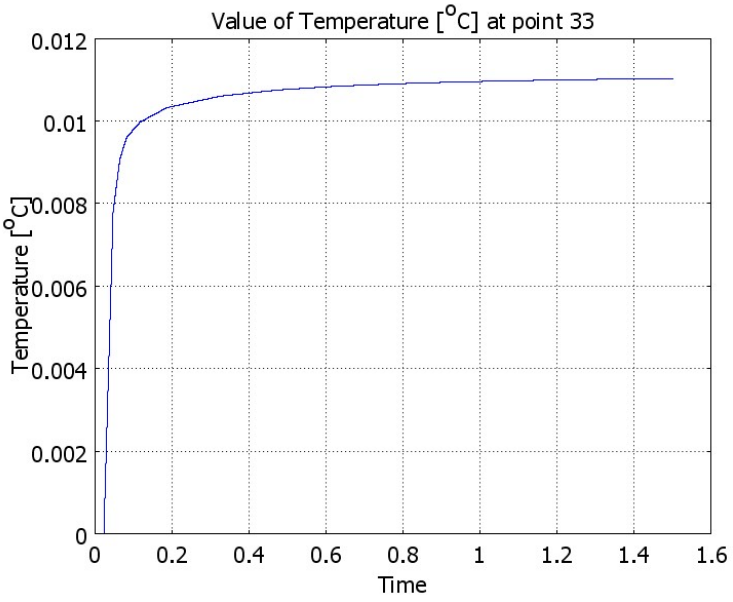


Figure 4.13. 3D FEM simulation result for Design C1's rise time in water.

In order to show that the designed micro-stages' and cantilevers' rise times would match with each other, they are coupled together in water with 3D FEM simulation as shown in Figure 4.14 and Figure 4.15. For the coupled model, MLCT-C type cantilever is coupled with Design C5. In the coupled simulation, fluid boundaries and anchor pads of the micro-stage are fixed at 0°C, boundary under the membrane is insulation symmetry and heat flux of 1000 W/m$^2$ is given to the up and bottom surfaces of the mid-plate that is drawn 0.5 $\mu$m down from cantilever' tip and 0.5 $\mu$m up from the membrane's top surface.

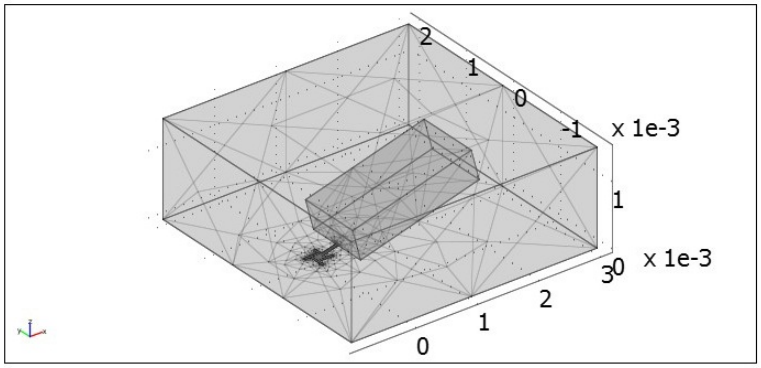


Figure 4.14. 3D FEM simulation of coupled MLCT-C type cantilever and Design C5.

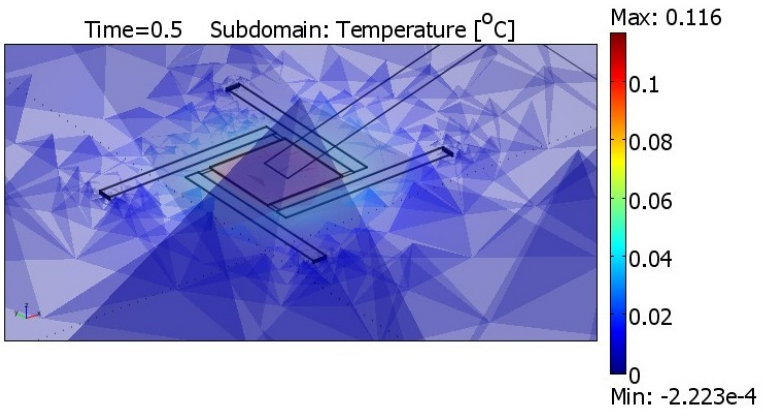


Figure 4.15. 3D FEM simulation result of coupled MLCT-C type cantilever and Design C5 for heat transfer.

Before coupling them, MLCT-C had a rise time of 30 ms in water that is shown in Figure 2.9 and Design C5 had a rise time of 60 ms in water that can be find in appendix and shown in Figure E.6. Design C5 is designed to thermomechanically match with MLCT-C type cantilever and before the coupled model their rise times in water were designed to have same order of magnitudes. With the coupled model in 3D FEM simulation in water, tip of the cantilever has rise time of 53 ms as shown in Figure 4.16, while Design C5 has 51 ms in the mid-point of its membrane as shown in Figure 4.17. Rise time of MLCT-C type cantilever and Design C5 micro-stage is nearly same in the coupled model and thermal deflection of Design C5 also matches with MLCT-C type cantilevers as shown in Figure 2.1 and Figure D.7 that it gives thermomechanically matched cantilever/MEMS pair as it was expected. Summary of rise times of MLCT-C type cantilever and the coupled Design C5 micro-stage in fluid are also shown in the Table 4.2 below.

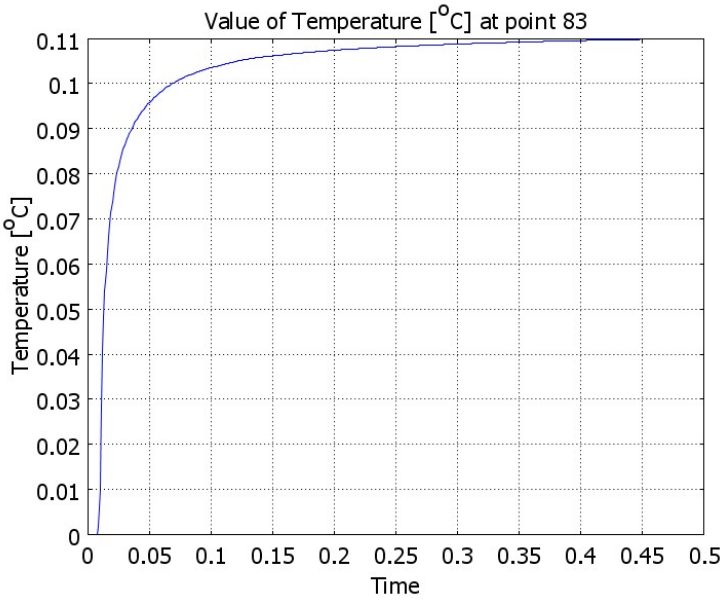


Figure 4.16. 3D FEM simulation result for the heat transfer of the coupled model in water, tip of the cantilever has a rise time 53 ms.

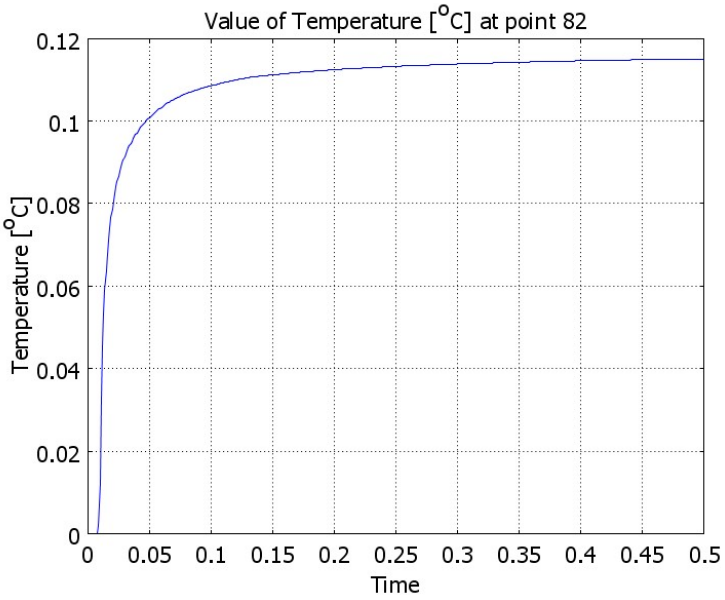


Figure 4.17. 3D FEM simulation result for the heat transfer of the coupled model in water, mid-point of the micro-stage's membrane has a rise time 51 ms.

Table 4.2. Summary of rise times of MLCT-C type cantilever and the coupled Design C5 micro-stage in fluid.

| | **In air** | **In water** |
|---|---|---|
| **Analytical, cantilever away from boundary** | 7 ms | |
| **FEM, cantilever away from boundary** | 8 ms | 30 ms |
| **FEM, cantilever on top of a Ti-membrane stage** | 1.8 ms | 15 ms |
| **FEM, Design C5 micro-stage** | | 60 ms |
| **FEM, cantilever (coupled with Design C5 micro-stage)** | | 53 ms |
| **FEM, Design C5 micro-stage (coupled with cantilever)** | | 51 ms |

### 4.1.4. Stiffness

In 3D FEM simulation to find the stiffness of Design C1, 1N force to the specified point in the Figure 4.7 is applied. With the applied force, micro-stage is deflected and from the Equation 4.1 where $F$ is the applied force, $x$ is the deflection and $k$ is the stiffness, stiffness is calculated as 0.5 N/m. Stiffness of MLCT-C type cantilever is given in Bruker's catalog as 0.01 N/m that Design C1 is 50 times stiffer than MLCT-C type cantilever.

$$k = \frac{F}{x} \tag{4.1}$$

In other 3D FEM simulations to find the stiffness (shown in appendix) of the other micro-stages, 1N force to the center point of the membranes is given and causes the micro-stages to deflect. Stiffness of the designed micro-stages that are calculated through the 3D FEM simulation results which are shown in Figures 4.18, 4.19 and 4.20 below. Stiffness of Design D1 and Design B1 are calculated as 1.7 N/m and 2 N/m, respectively. Stiffness of MLCT-D and MLCT-B type cantilevers are given in Bruker's catalog as 0.03 N/m and 0.02 N/m, respectively, that they are approximately 2 orders of magnitude stiffer than MLCT-D and MLCT-B type cantilevers. These numbers guarantee that the MEMS will not be affected by biomolecular forces as the micro-stages are much more stiffer than the cantilevers.

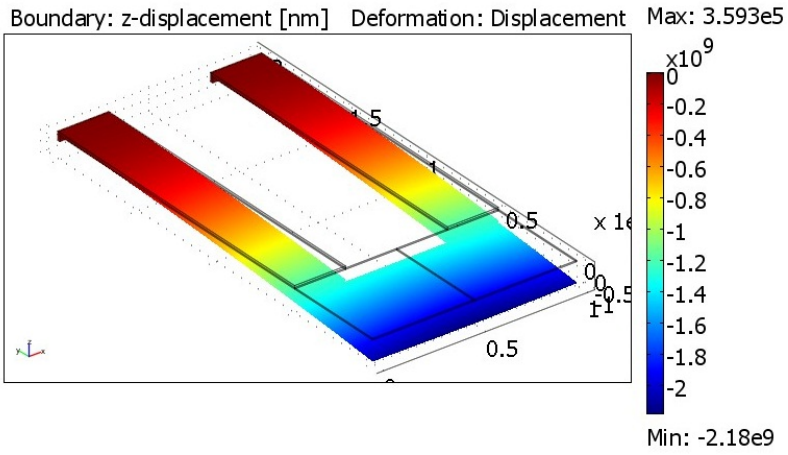


Figure 4.18. Deflection result of Design C1 as 1N force is given to the center point of membrane.

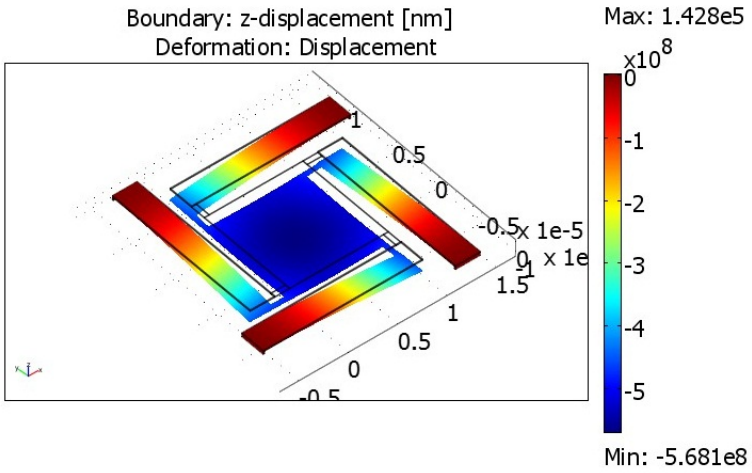


Figure 4.19. Deflection result of Design D1 as 1N force is given to the center point of membrane.

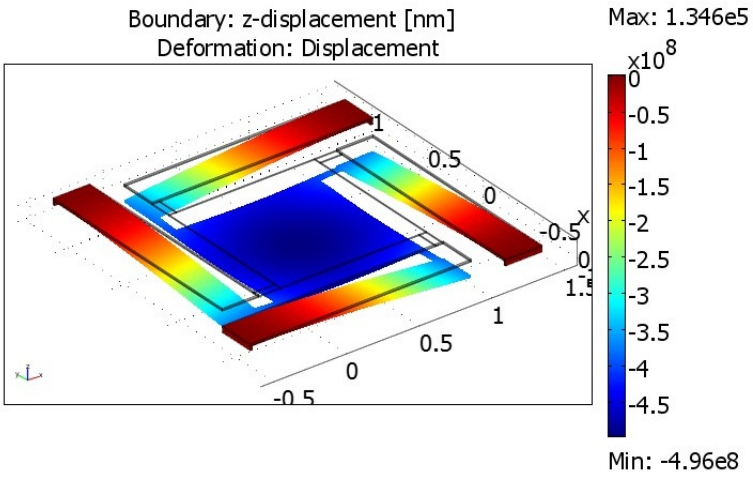


Figure 4.20. Deflection result of Design B1 as 1N force is given to the center point of membrane.

# 5. MICROFABRICATION OF MICRO-STAGES AND TESTING

The microfabrication of the designed micro-stages involves a 3-mask process as schematically illustrated in Figure G.1. Micro-stages are fabricated on Silicon (Si) wafer whereas standard IC materials Al and Ti are used for the structures and AZ5214E photoresist is used as a sacrificial layer.

## 5.1. Process Flow

Process flow of the designed micro-stages is shown in Figure 5.1 below.

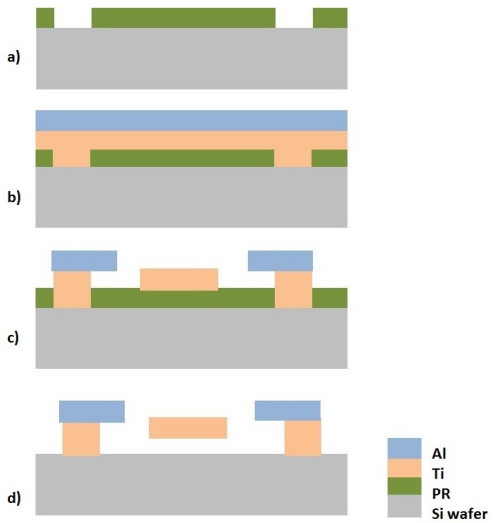


Figure 5.1. Schematics of process flow of the designed micro-stages. (a) Patterned photoresist as a sacrificial layer. (b) Metallization with sputter (Ti/Al). (c)Wet etching of the structure. (d) Releasing the micro-stage by removing the sacrificial layer.

The fabrication process starts with patterning the first mask (dark-field) that is shown in Figure G.2 to define the pads of micro-stages legs that are for anchoring the micro-stages to the Si wafer. In order to pattern the sacrificial PR for the anchor pads with the first mask, positive lithography is done with AZ5214 PR. The Si wafer substrate is spin coated at 4000 rpm with PR for 50 seconds with Cee200cbx spin coater. Soft bake is done in 110°C for 50 seconds and then UV exposure is done in 40 mj/cm$^2$ dose with soft contact mode with EVG620 contact aligner. After the exposure, development of PR is done in 4:1 DI: AZ400K developer for 50 seconds. Hard bake is done in 80 °C for 30 seconds. The patterned PR with the first mask is schematically shown in Figure 5.1a.

On the patterned sacrificial PR, sputtering is done for the structural layers. "DC and RF Magnetron Sputtering System" (Vaksis, Angora Magnetron Sputtering) for the metal sputtering is preheated to temperature 50°C in 2 hours initially. Then 0.6 $\mu$m Ti is sputtered with 200 watt DC coating power and for 2 times 60 minutes (time interval between two coating is 180 minutes). After the Ti sputtering the second metal layer, 0.9 $\mu$m Al is sputtered with 200 watt DC coating power and for 2 times 65 minutes (time interval between two coating is 180 minutes).

Ti and Al sputtered wafer after the PR-patterning is schematically shown in Figure 5.1b. In order to define the legs of the micro-stages, positive photolithography is done with the second mask (clear-field) that is shown in Figure G.3. Ti and Al sputtered wafer is spin coated at 4000 rpm with PR for 50 seconds. Soft bake is done in 110°C for 50 seconds and then UV exposure is done in 40 mj/cm$^2$ dose with soft contact mode. After the exposure, development of PR is done in 4:1 DI: AZ400K developer for 50 seconds. Hard bake is done in 80 °C for 30 seconds. Microscopy image of the developed wafer after the lithography with the second mask is shown in the Figure 5.2 below.

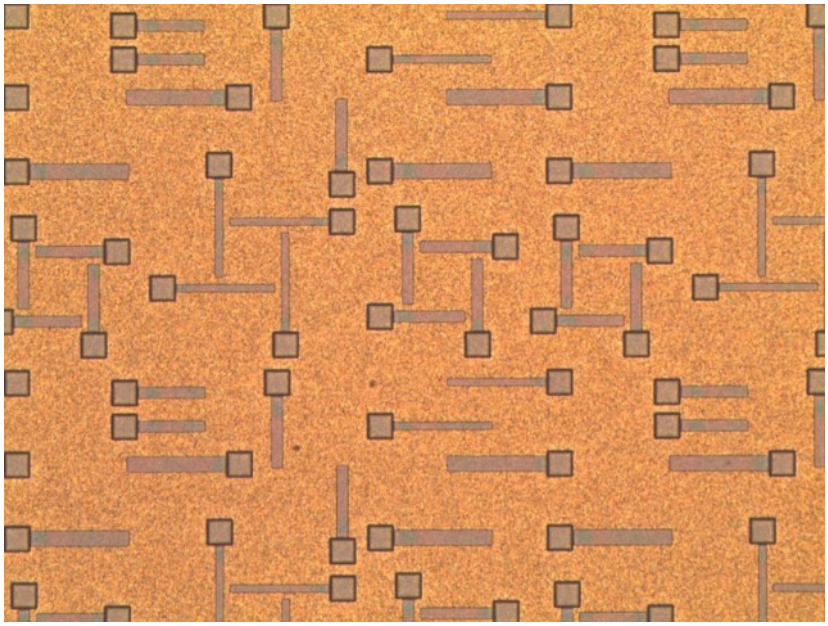

Figure 5.2. Microscopy image of the developed wafer after the lithography with the second mask.

After the second lithography, Al is etched with Al etchant at 50°C, 16:2:1:1 $H_2O$: $HNO_3$: $CH_3COOH$ [21, 22], for 1 minute. The Al etched wafer after the second lithography is shown in Figure 5.3.

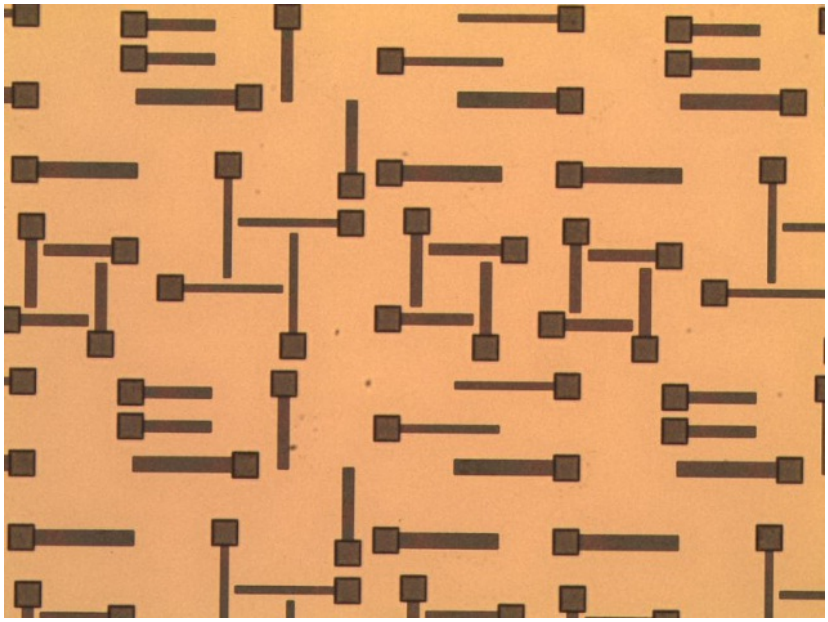

Figure 5.3. Microscopy image of the Al etched wafer after the lithography with the second mask.

The patterned PR with the second lithography is then removed with 5 seconds of acetone bath, 5 seconds of IPA bath and lastly washed by DI water; the wafer after the process is shown in the Figure 5.4.

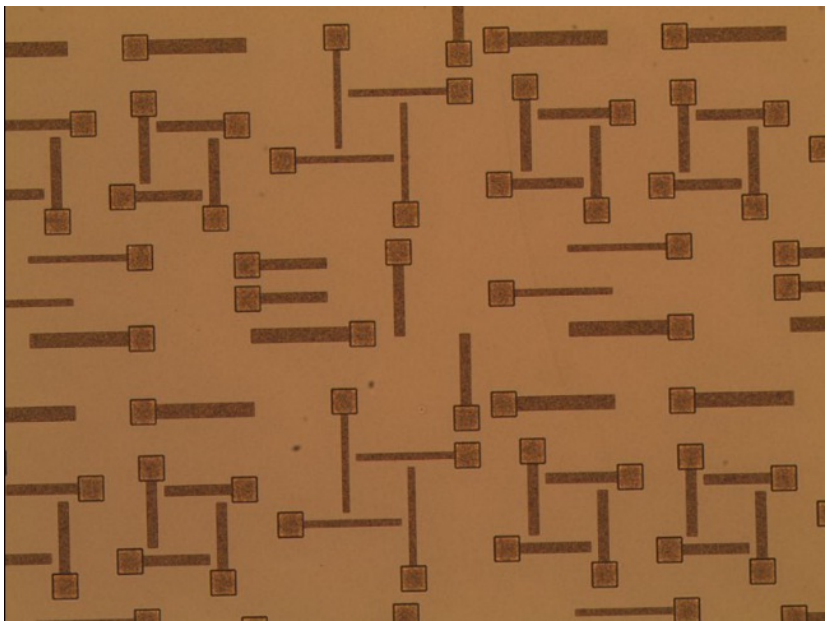

Figure 5.4. Microscopy image of the Al etched wafer after the lithography with the second mask and after acetone/IPA bath.

The third lithography (positive) is done to define the second layer of the legs and the Ti membranes of the micro-stages with the third mask (clear-field) that is shown in Figure G.4. Wafer is spin coated at 4000 rpm with PR for 50 seconds. Soft bake is done in 110°C for 50 seconds and then UV exposure is done in 40 mj/cm$^2$ dose with soft contact mode. After the exposure, development of PR is again done in 4:1 DI: AZ400K developer for 50 seconds. Hard bake is done in 80 °C for 30 seconds. Microscopy images of the developed wafer after the lithography with the third mask are shown in the Figure 5.5 and Figure 5.6 below.

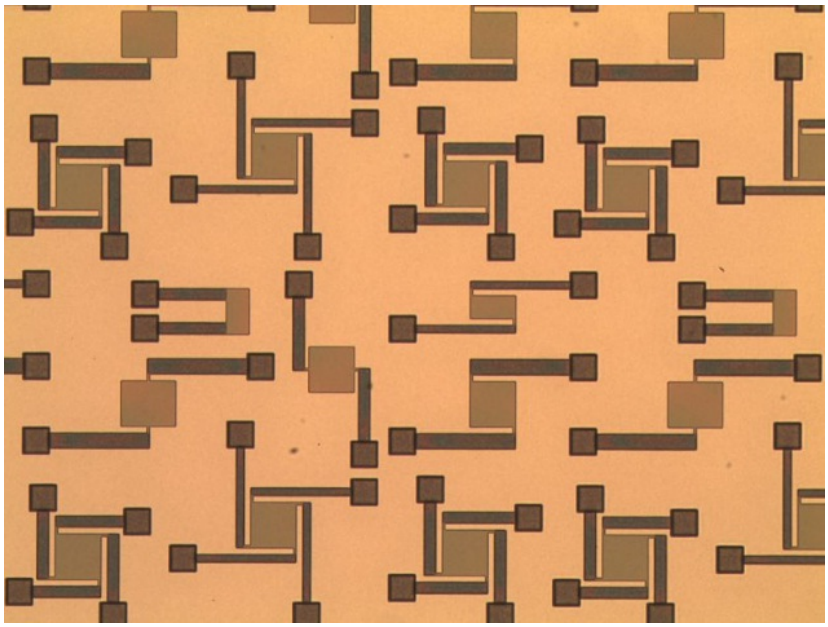

Figure 5.5. Microscopy image of the developed wafer after the lithography with the third mask.

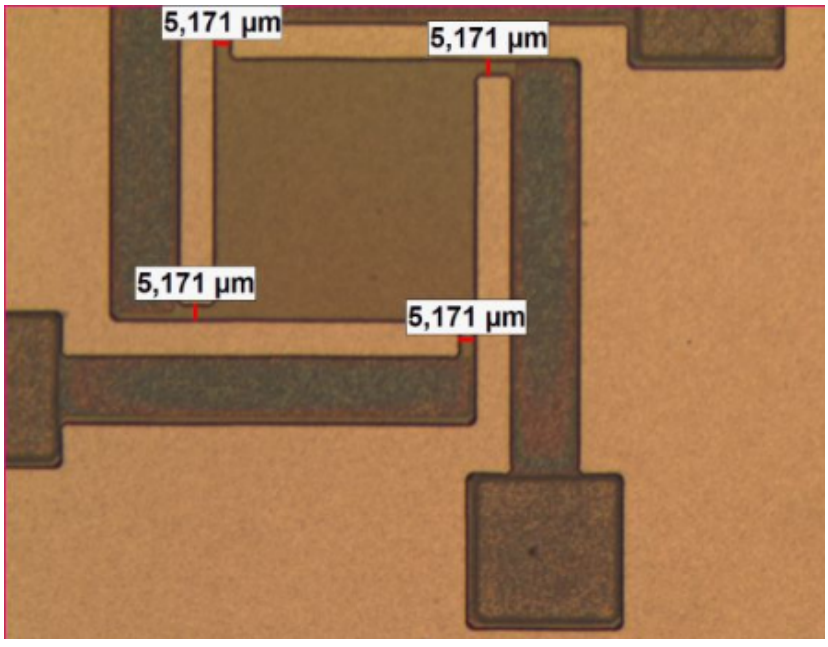


Figure 5.6. Microscopy image of the developed wafer after the lithography with the third mask, in detail.

After the third lithography, Ti is etched with Ti etchant, 20:1:1, $H_2O$: $H_2O_2$: HF [21, 22] for 20 seconds. Wafer after the Ti etching is shown schematically in Figure 5.1c and the Ti etched wafer after the third lithography is shown in Figure 5.7 and Figure 5.8 below in detail.

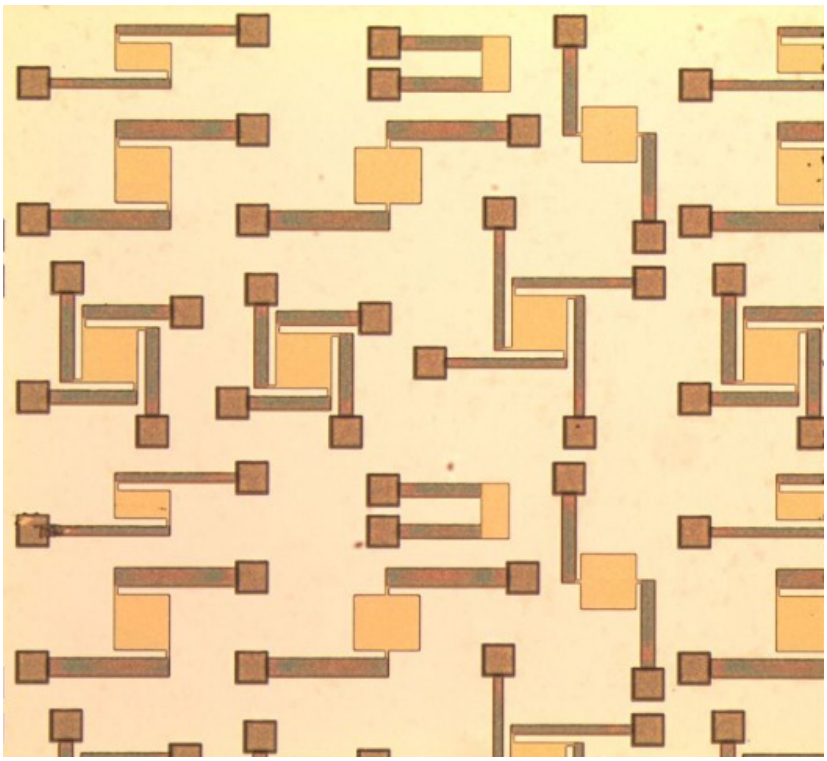

Figure 5.7. Microscopy image of the Ti etched wafer after the lithography with the third mask, in detail.

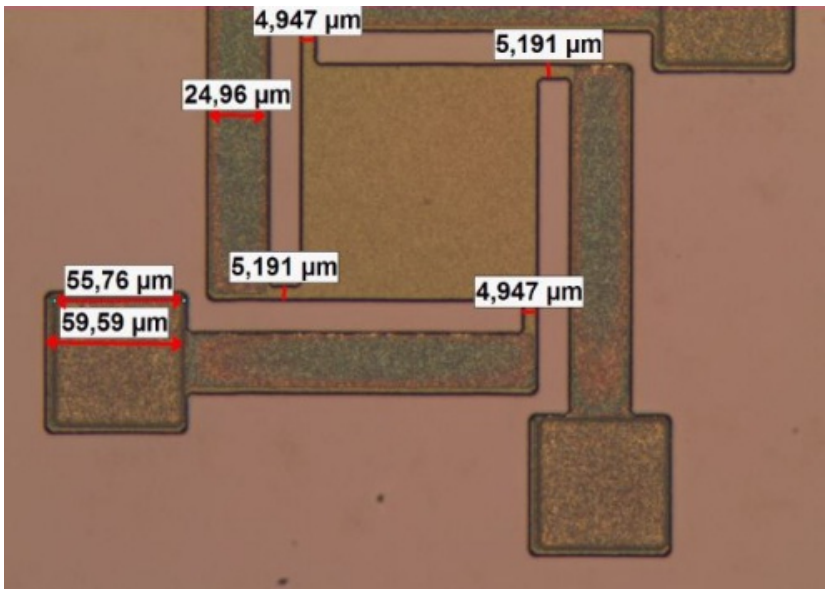


Figure 5.8. Microscopy image of the Ti etched wafer after the lithography with the third mask, in detail.

Finally the micro-stages are put into the asher (AP-300 Plasma System, Nordson MARCH) with 250 Watt RF power, 50 sccm $O_2$ flow rate. The released micro-stage is schematically shown in Figure 5.1 (d). Microscopy images of the micro-stages after 40 minutes in the asher are shown in Figure 5.9 and Figure 5.10 below.

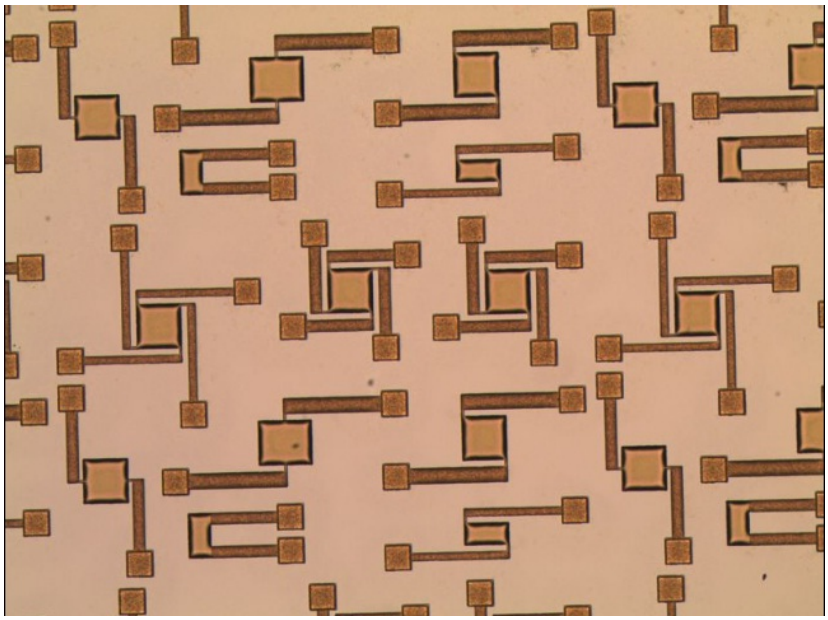

Figure 5.9. Microscopy images of the micro-stages after 40 minutes in the asher.

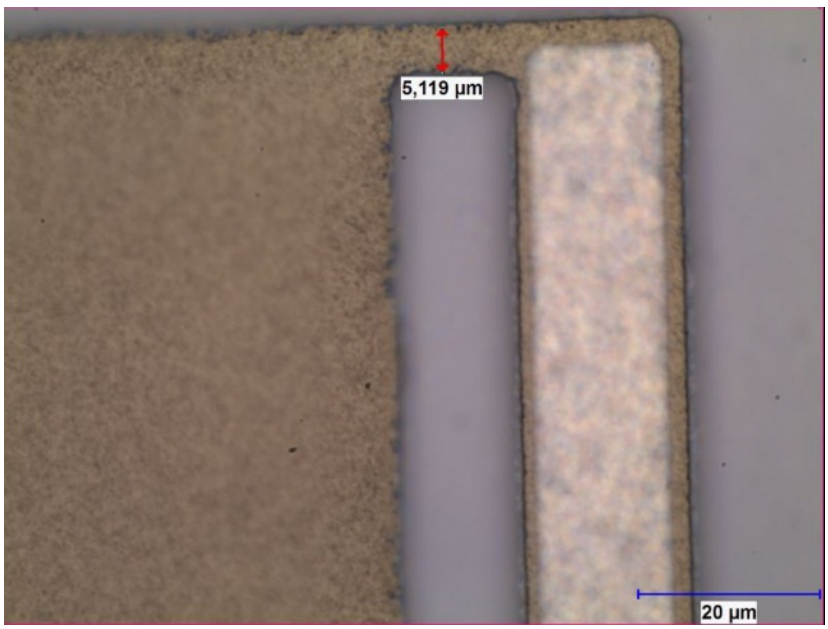


Figure 5.10. Microscopy images of the micro-stages after 40 minutes in the asher, in detail.

After 3 hours in the asher, microscopy images of the micro-stages are shown in Figure 5.11 below.

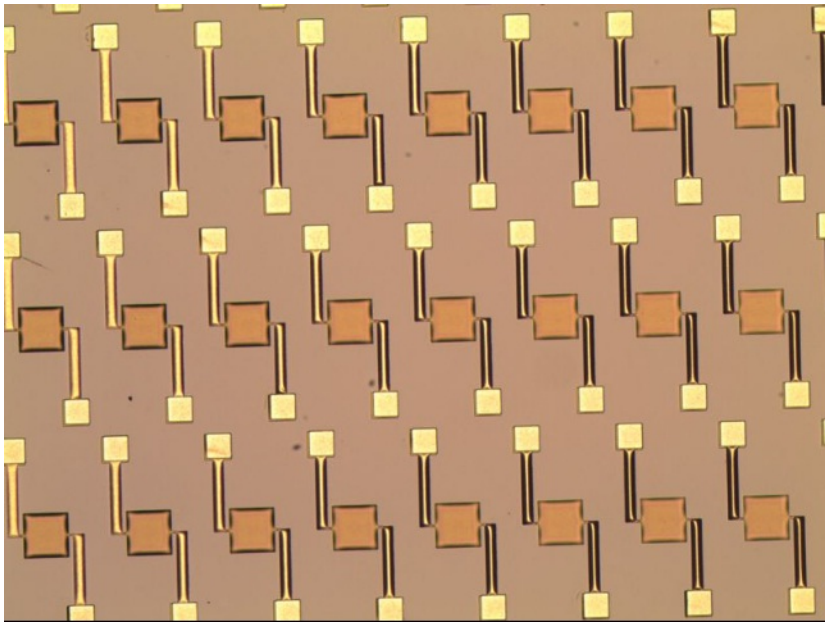

Figure 5.11. Microscopy images of the micro-stages after 3 hours in the asher.

## 5.2. Micro-stages' Characterization in AFM

AFM is employed as surface profiler and by scanning the bimaterial leg of a micro-stage, scanned region can be seen in Figure 5.12a, thickness of micro-stage's bimaterial leg is measured as approximately 3 $\mu$m as shown in Figure 5.12b and with 1.4 $\mu$m PR and 1.5 $\mu$m metal thickness it is possible. From the leg profile it can be understood that micro-stages did not collapsed.

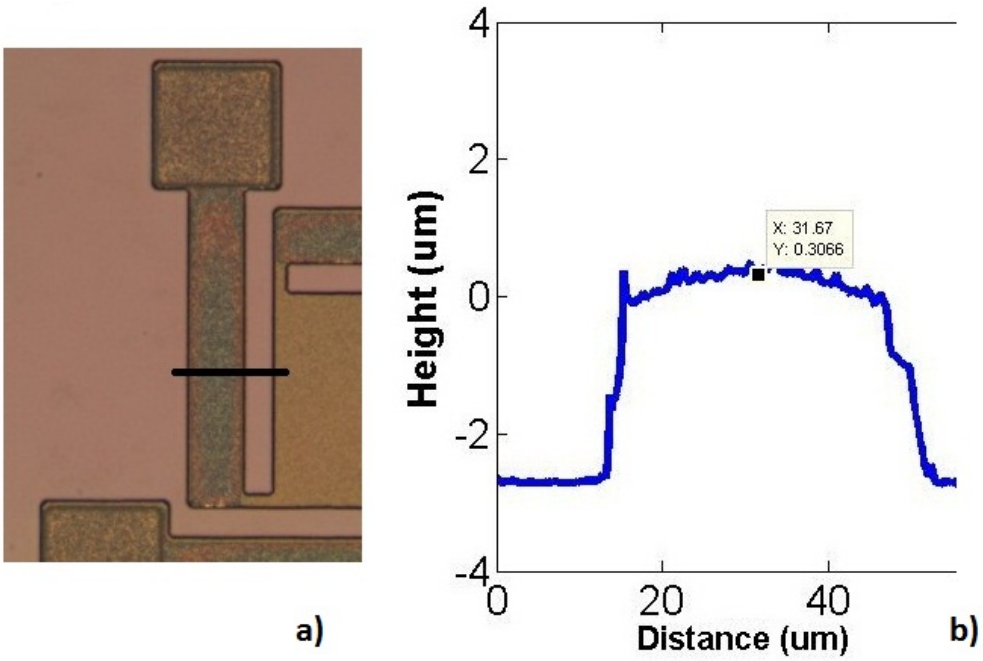


Figure 5.12. Scanned region (a) and leg profile (b) of micro-stages after 40 minutes in the asher.

The fabricated devices are characterized for their spring constants by AFM. For the experiment Bruker's SNL-10 type C cantilever is used. Cantilever is pushed to the hard surface to measure the deflection sensitivity data and deflection sensitivity on hard surface is recorded as 0.0380 $\mu$m/V.

By landing on the micro-stage membrane with the calibrated SNL-10 type C cantilever, deflection sensitivity of micro-stage membrane can be calculated from the force curve [23]. Spring constant of the micro-stage membrane can be calculated by comparing the deflection sensitivity that is taken from the hard surface with deflection sensitivity that is taken from the micro-stage membrane. Indeed, finite spring constant of the micro-stage can be calculated if the deflection sensitivity that is taken from micro-stage membrane is different from the deflection sensitivity that is taken from the hard surface. Calculation method of micro-stage's spring constant from cantilever's landing on hard surface and then micro-stage's membrane is explained by

$$F = k.S.V_x \tag{5.1}$$

where $F$ is the force between the tip and sample, $k$ is the cantilever/micro-stage spring constant, $V_x$ is the measured cantilever's deflection in volt, and $S$ is the deflection sensitivity. The deflection $V$ is measured directly with a photodiode [24] and is same on both surfaces. By equalizing $k_{cant}.S_{hardsurface}$ to equivalent spring constant ($k_{cant}$ in series with $k_{memb}$) multiplied by $S_{memb}$,

$$k_{memb} = \frac{S_{hardsurface}}{S_{memb} - S_{hardsurface}} k_{cant} \tag{5.2}$$

is obtained. In our case sensitivity data taken from the micro-stage is measured approximately same as the hard surface and as it is seen from the equations above it is not possible (denominator can not go to zero), so it is understood that micro-stages are not released yet. This might be due to excessive heat on PR sacrificial layer or residual stress built up on the layers. An alternative approach can be stripping the sacrificial PR using acetone or PR remover. This approach also requires super critical dryer to prevent stiction.

Spring constant of the specific AFM cantilever is calibrated using thermal noise spectrum acquired by the system. With the thermal tune method in AFM, frequency spectrum of the cantilever is estimated and by fitting the frequency spectrum to a Lorentzian line shape the AFM software arrives at an estimate of the cantilever's spring constant [25]. With the thermal tune method resonance frequency of the cantilever is recorded as 43.69 kHz as shown in the Figure 5.13 below and with the deflection sensitivity that was recorded spring constant of the cantilever is recorded as 0.4577 N/m.

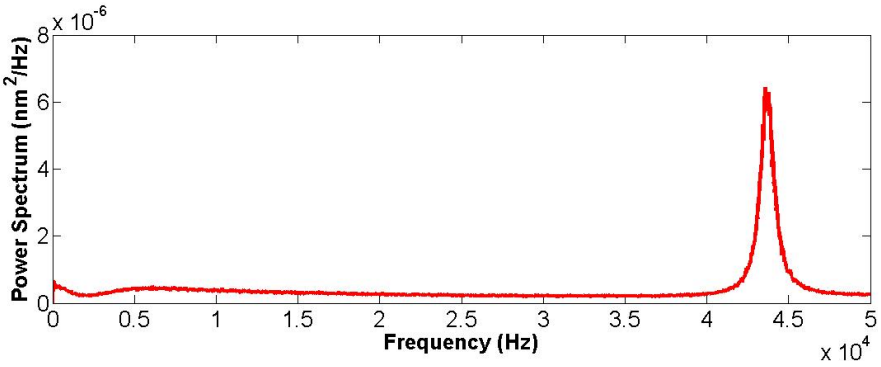


Figure 5.13. Graph of cantilever's thermal spectrum, shows the resonance frequency of the cantilever.

# 6. CONCLUSION

This thesis reports the design and fabrication of micro-stages that are thermomechanically matched with cantilevers in order to compensate the thermal drift in AFM cantilevers. The development of the micro-stages consists of: (i) Cantilevers' thermomechanical analysis; (ii) Design of the optical readout setup; (iii) Design and microfabrication of the micro-stages.

(i) Cantilevers' thermomechanical analysis: Steady state thermal deflections, dynamic operation of the cantilevers are analyzed by analytical modeling and FEM simulations.

(ii) Design of the optical readout setup: To validate the results of the analytical modeling of the cantilever, experimental setup is used. The thermal deflection of the MLCT-C type cantilever in air, which is calculated with analytical model and also found with 2D FEM simulation, is validated with the optical characterization setup experiments. The discrepancy between the analytical calculations and the experimental result is approximately 15%. FEM predicts thermal induced displacement with 14.5% error as compared to experimental result. MLCT-C type cantilever deflection is calculated as 339 nm/K and the compensating designed micro-stage's (Design C1) deflection is simulated with 3D FEM as 299 nm/K. For 1°C change in temperature MLCT-C type cantilever's thermal deflection corresponds to 33.9 pN force but coupling the cantilever with micro-stage the differential thermal deflection corresponds to 4 pN. Dynamic operation results of the coupled MLCT-C type cantilever and Design C5 micro-stage are 53 ms and 51 ms, respectively. Indeed, with the designed micro-stages there is improvement on thermal drift in AFM cantilevers.

(iii) Design and microfabrication of the micro-stages: According to the analytical,

FEM simulation and experimental results micro-stages are designed and fabricated by surface micromachining technology. Various micro-stages for different types of cantilevers are designed in this thesis. These micro-stages are fabricated at Microsystem Based Medical Device Development Center of Bogazici University Life Sciences and Research Center using surface micromachining technology. This fabrication process was the first process that was done in Microsystem Based Medical Device Development Center of Bogazici University Life Sciences and Research Center. With this thesis Al and Ti deposition/ wet etching, lithography and dry etching processes are characterized.

Recommendations:

- Thermal time constant could not be calculated through the optical setup as TEC limited the rise time. An alternative method can be heating the cantilever's tip with a laser diode instantly with a new setup. By mounting the laser diode on a manipulator with movement ability in x, y, and z directions cantilever tip can be heated precisely [26].

- Releasing of the fabricated devices needs further process optimization. Supercritical dryer will be used after stripping the sacrificial PR with acetone or PR remover to prevent the stiction problem as releasing the micro-stages.

- Different material combinations can be evaluated. As Al and Ti mismatch of CTE is not high, with higher mismatch of CTE in micro-stages shorter bimaterial legs and stiffer micro-stage design is possible.

# APPENDIX A: MLCT-D AND MLCT-B TYPE CANTILEVERS' THERMAL DEFLECTIONS

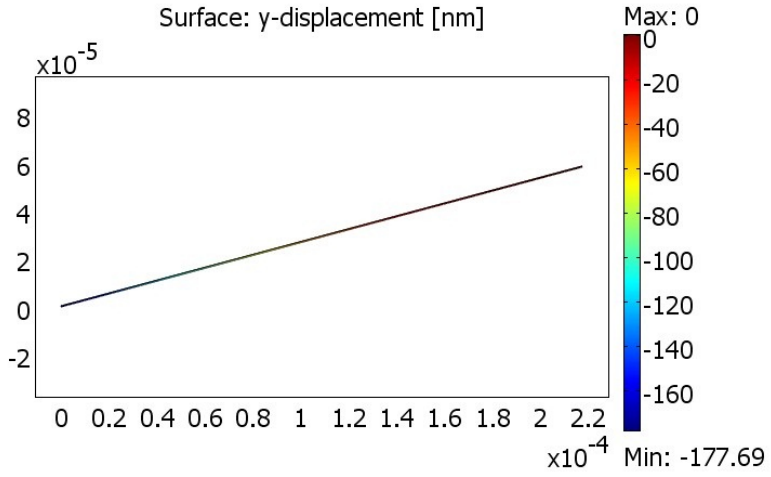


Figure A.1. 2D FEM simulation for the deflection analysis of D type cantilever.

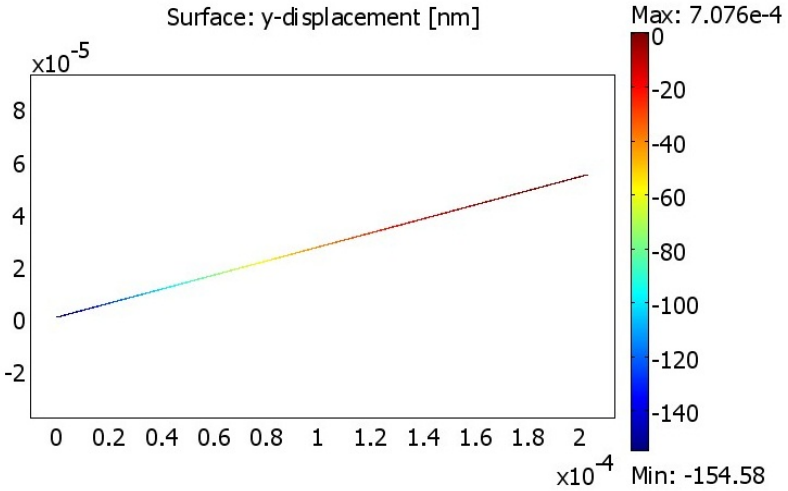


Figure A.2. 2D FEM simulation for the deflection analysis of B type cantilever.

# APPENDIX B: MLCT-D AND MLCT-B TYPE CANTILEVERS' HEAT TRANSFER

MLCT-D type cantilever's rise time in air is calculated as 0.0044 s on the tip with the analytical model where with 2D FEM, as shown in the Figure B.1 and B.2, is given as 0.0023 s. As in the MLCT-C's and MLCT-B's 2D FEMs, MLCT-D cantilever is also modeled as staying on top of a Ti micro-stage with an angle of 15 but in the analytical model cantilever/micro-stage interaction is not considered.

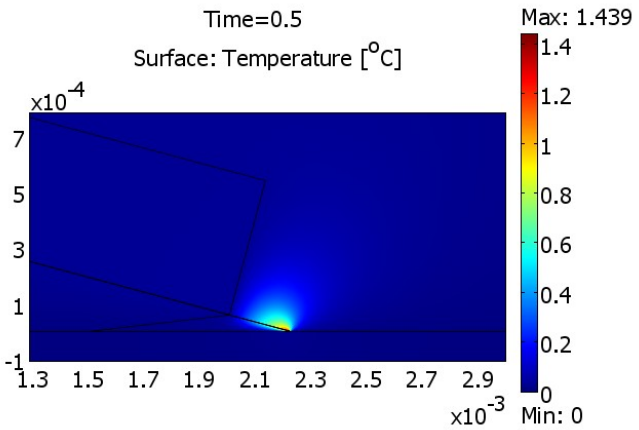


Figure B.1. 2D FEM for MLCT-D type cantilever's rise time in air.

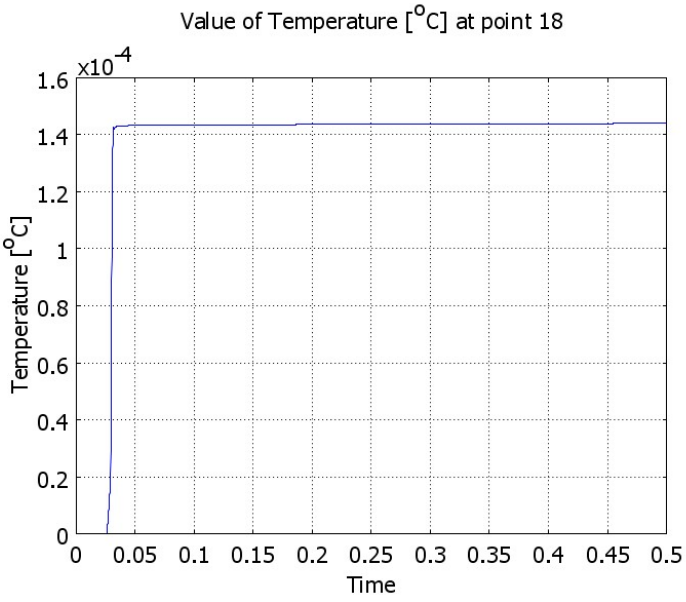


Figure B.2. 2D FEM simulation result for MLCT-D type cantilever's rise time on tip in air.

The 2D FEM for the rise time simulation of MLCT-D type cantilever tip and the graph of temperature vs. time of the cantilever's tip in water are shown in the Figure B.3 and B.4. From the graph, the rise time is calculated as 0.018 s.

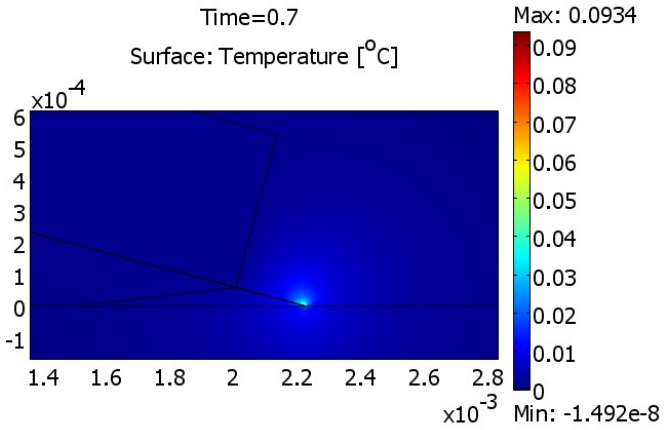


Figure B.3. 2D FEM for MLCT-D type cantilever's rise time in water.

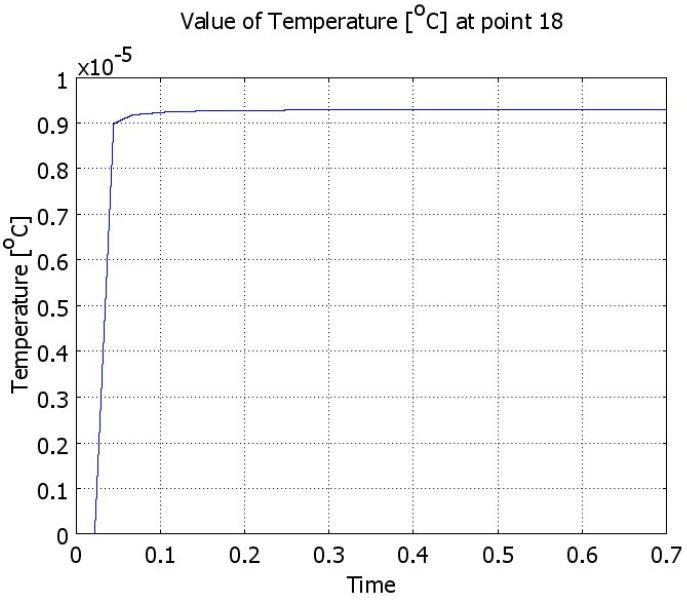


Figure B.4. 2D FEM simulation result for MLCT-D type cantilever's rise time on tip in water.

MLCT-B type cantilever's rise time in air is calculated as 0.0039 s on the tip with the analytical model where with 2D FEM, as shown in the Figures B.5 and B.6, is given as 0.0016 s. As in the MLCT-C's 2D FEM, MLCT-B cantilever is also modeled as staying on top of a Ti micro-stage with an angle of 15 but in the analytical model cantilever/micro-stage interaction is not considered.

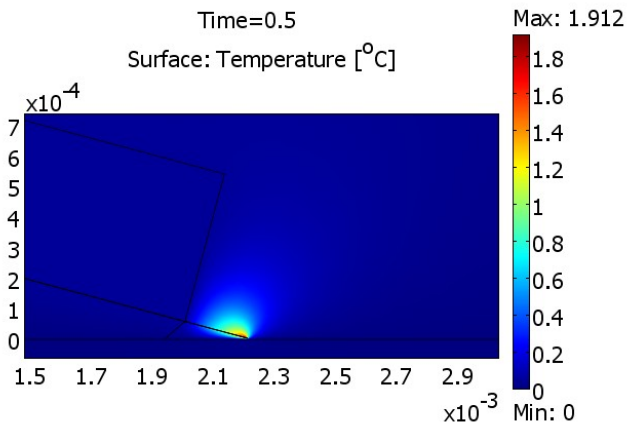


Figure B.5. 2D FEM for MLCT-B type cantilever's rise time in air.

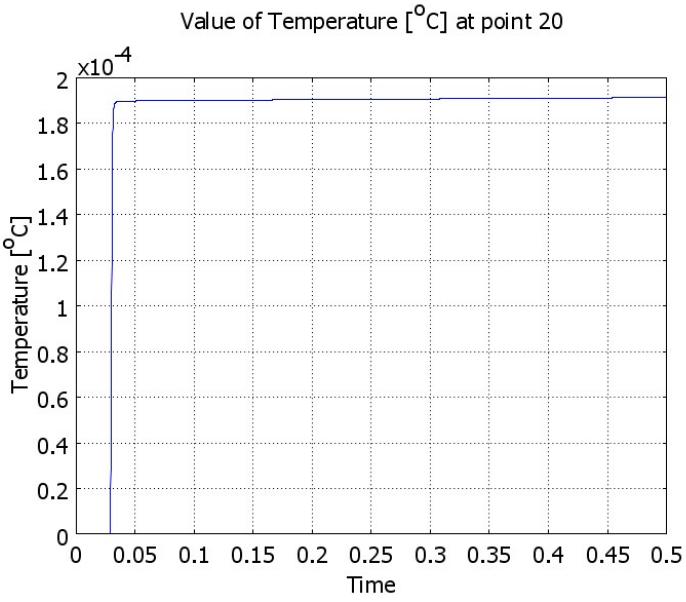


Figure B.6. 2D FEM simulation result for MLCT-B type cantilever's rise time on tip in air.

The 2D FEM for the rise time simulation of MLCT-B type cantilever tip and the graph of temperature vs. time of the cantilever's tip in water are shown in the Figures B.7 and B.8. From the graph, the rise time is calculated as 0.017 s.

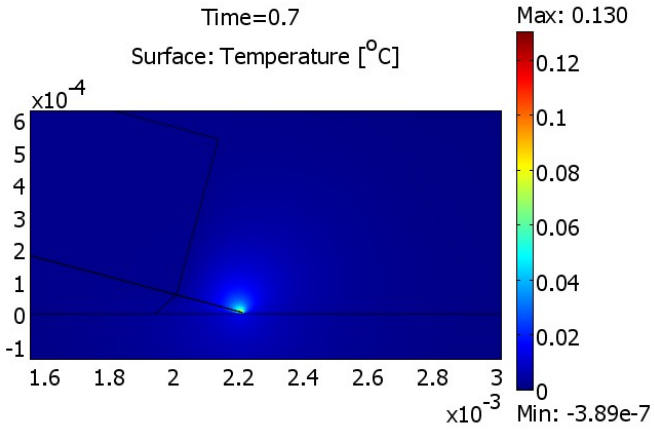


Figure B.7. 2D FEM for MLCT-B type cantilever's rise time in water.

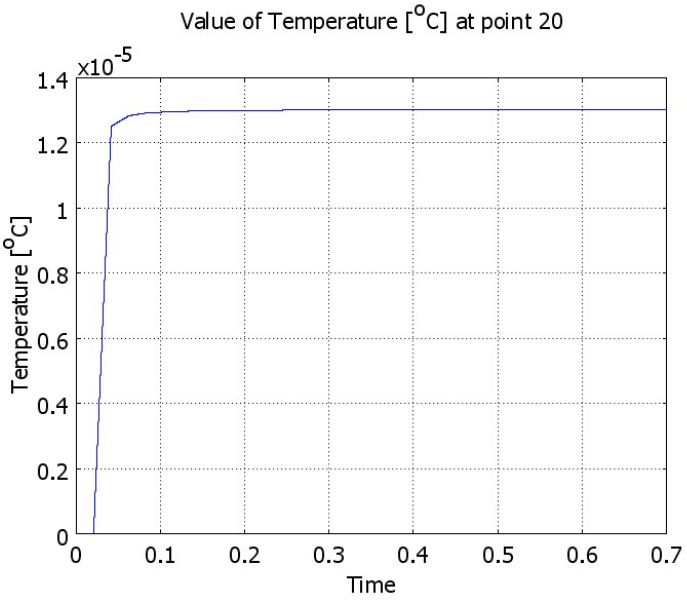


Figure B.8. 2D FEM simulation result for MLCT-B type cantilever's rise time on tip in water.

# APPENDIX C: DIMENSIONS OF OTHER MICRO-STAGES

Dimensions of other designed micro-stages for MLCT-C type cantilever are shown in the Figures C.1 - C.4 below.

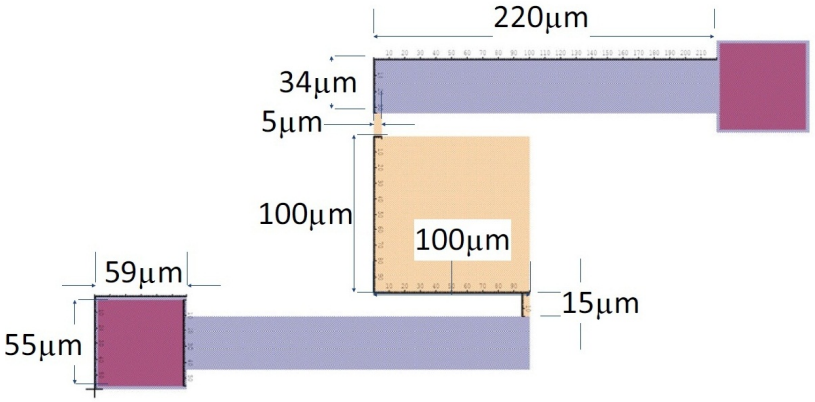


Figure C.1. Dimensions of Design C2.

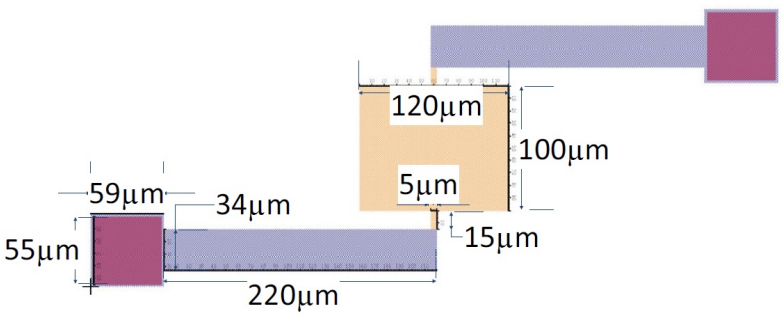


Figure C.2. Dimensions of Design C3.

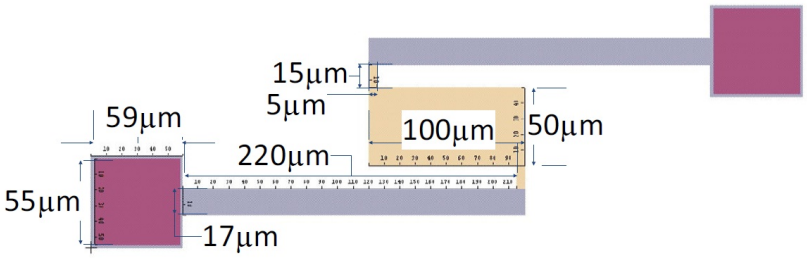


Figure C.3. Dimensions of Design C4.

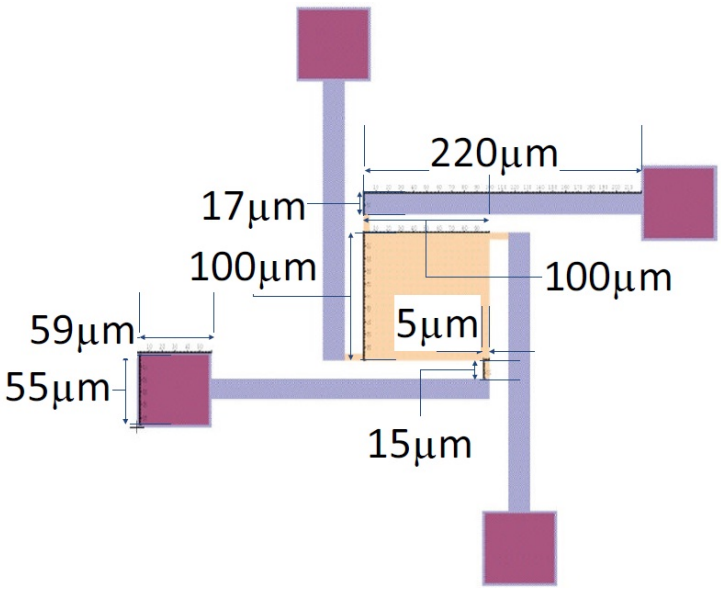


Figure C.4. Dimensions of Design C5.

Dimensions of other designed micro-stage for MLCT-D type cantilever is shown in Figure C.5 below.

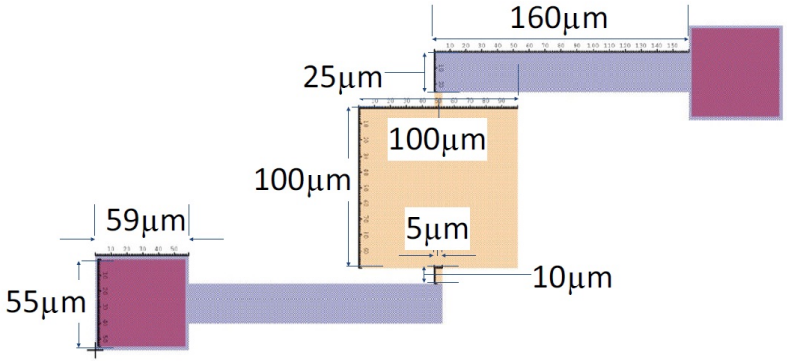


Figure C.5. Dimensions of Design D2.

# APPENDIX D: DEFLECTION OF OTHER MICRO-STAGES

3D FEM simulation results for deflection of the micro-stages are shown in Figure D.1, D.3, D.5, D.7 and D.9. Deflection of Design C2, Design C3, Design C4, Design C5 and Design D2 are 328 nm/K, 336 nm/K, 280 nm/K, 304 nm/K and 172 nm/K, respectively.

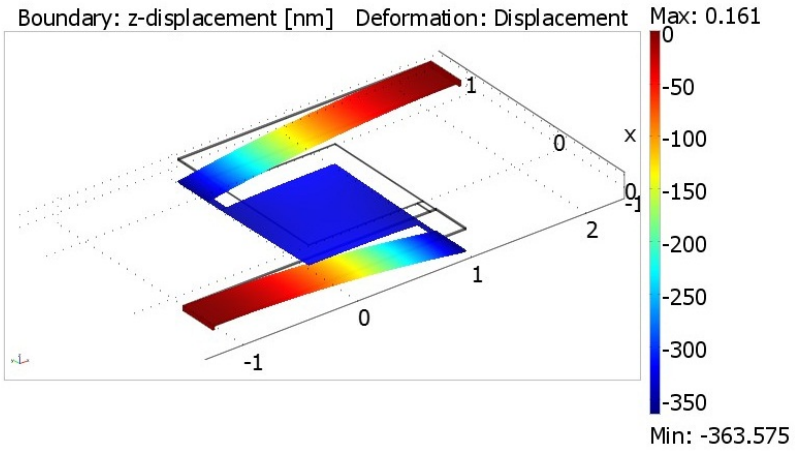


Figure D.1. Thermal deflection simulation result in 3D FEM for Design C2.

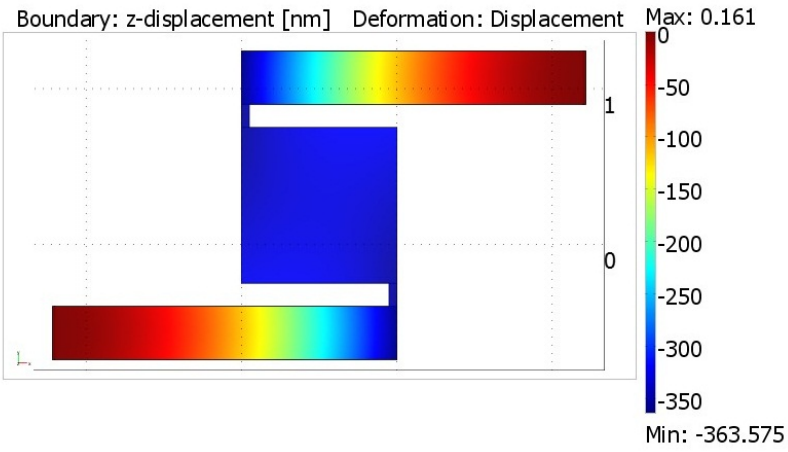


Figure D.2. Thermal deflection simulation result in 3D FEM for Design C2, top view.

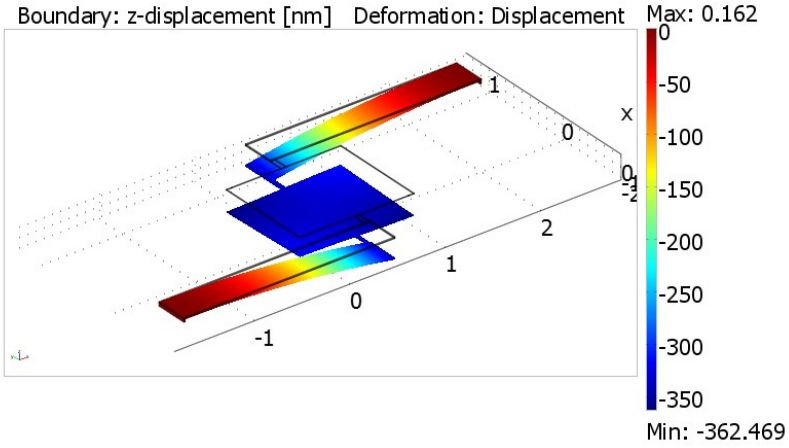


Figure D.3. Thermal deflection simulation result in 3D FEM for Design C3.

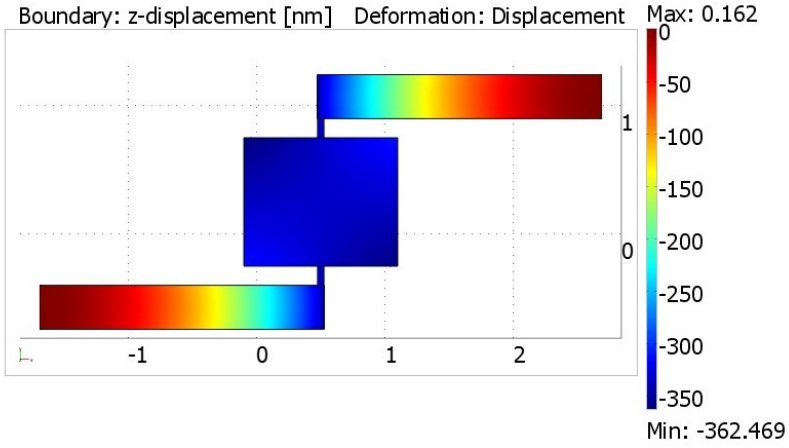


Figure D.4. Thermal deflection simulation result in 3D FEM for Design C3, top view.

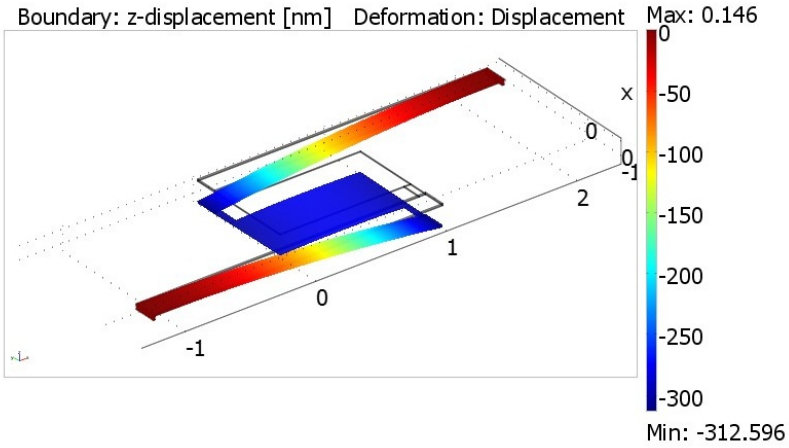


Figure D.5. Thermal deflection simulation result in 3D FEM for Design C4.

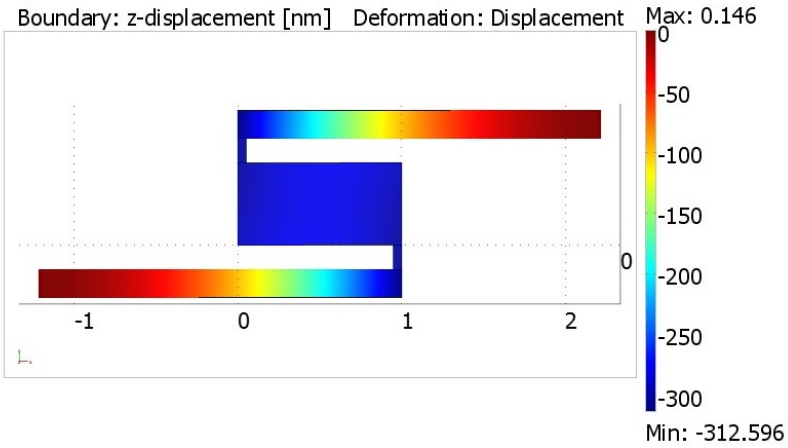


Figure D.6. Thermal deflection simulation result in 3D FEM for Design C4, top view.

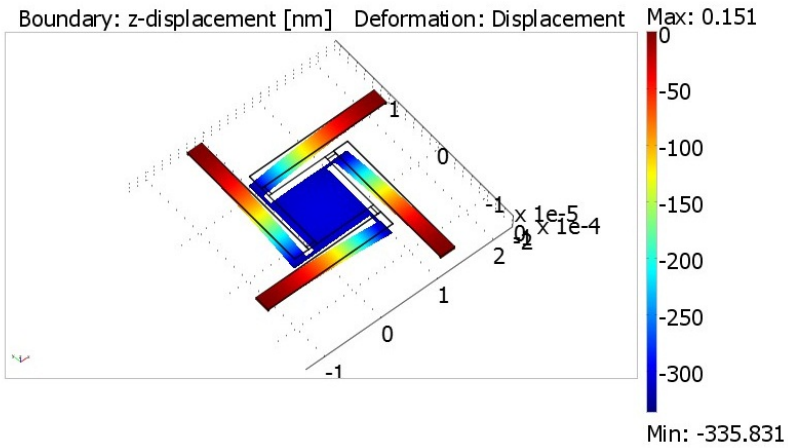


Figure D.7. Thermal deflection simulation result in 3D FEM for Design C5.

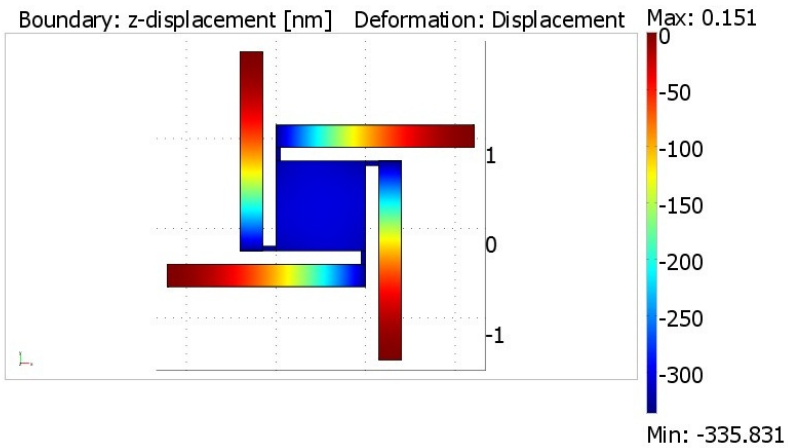


Figure D.8. Thermal deflection simulation result in 3D FEM for Design C5, top view.

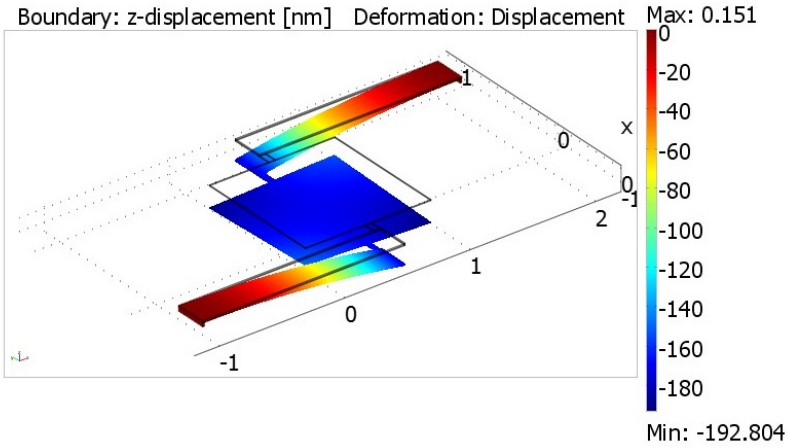


Figure D.9. Thermal deflection simulation result in 3D FEM for Design D2.

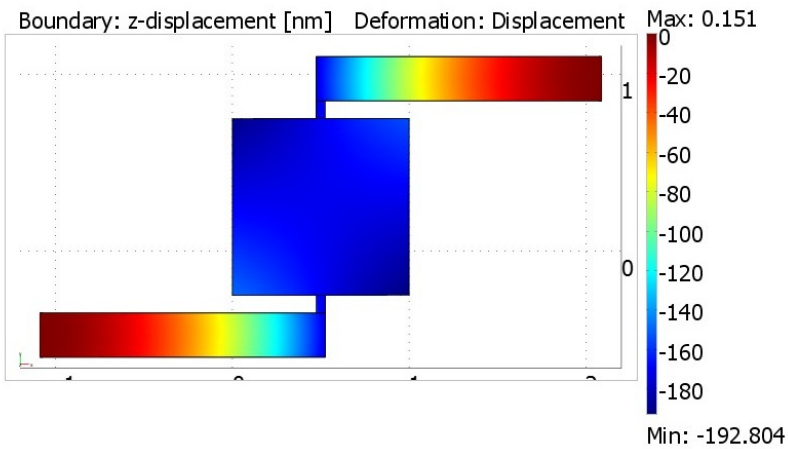


Figure D.10. Thermal deflection simulation result in 3D FEM for Design D2, top view.

# APPENDIX E: HEAT TRANSFER OF OTHER MICRO-STAGES

3D FEM simulation results for heat transfer of Design C2 in air and in water, Design C4 in air and in water are shown in Figure E.1, E.2, E.3 and E.4, respectively. Rise time of Design C2 in air is 2.8 ms, in water 66 ms while rise time of C4 in air is 2.1 ms and in water 43 ms.

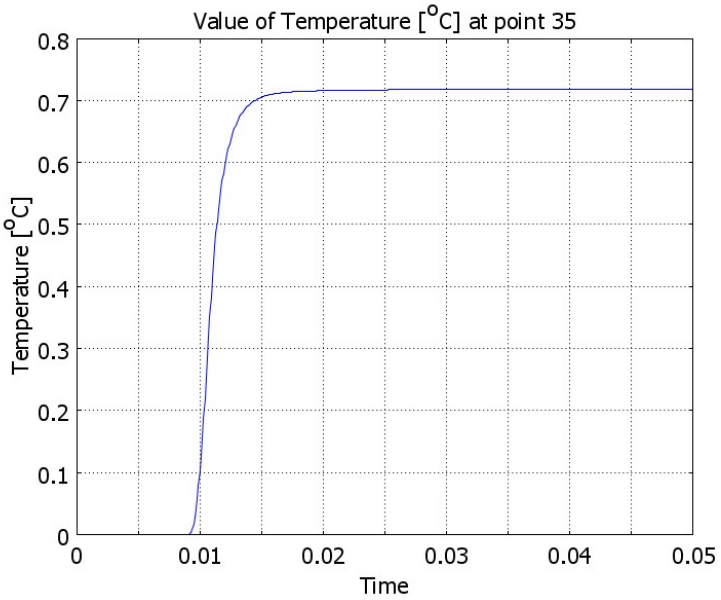


Figure E.1. 3D FEM simulation result for Design C2's rise time in air.

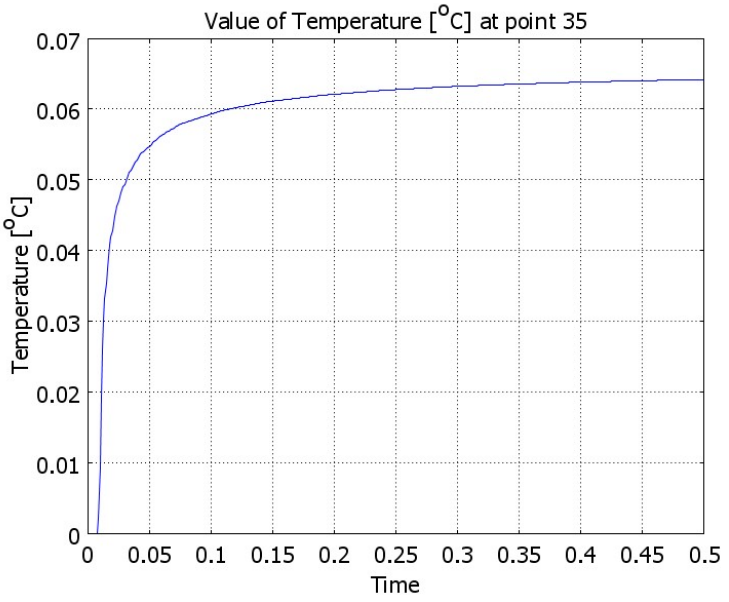


Figure E.2. 3D FEM simulation result for Design C2's rise time in water.

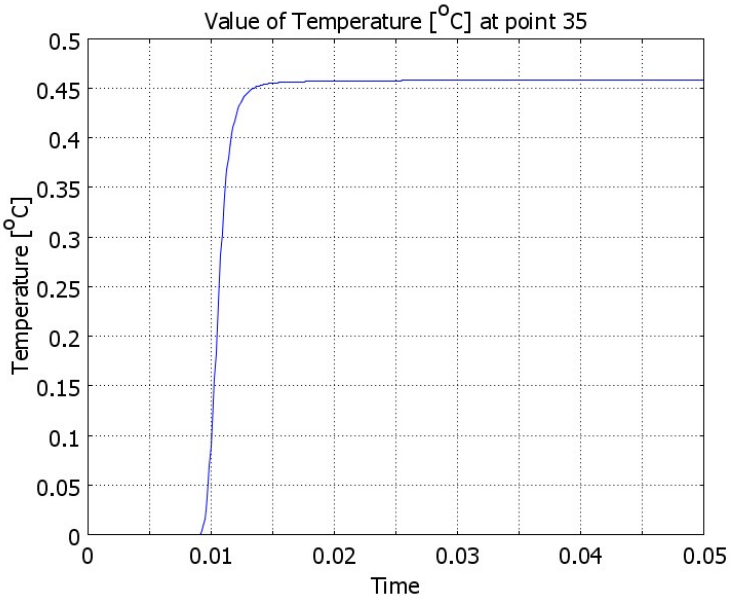


Figure E.3. 3D FEM simulation result for Design C4's rise time in air.

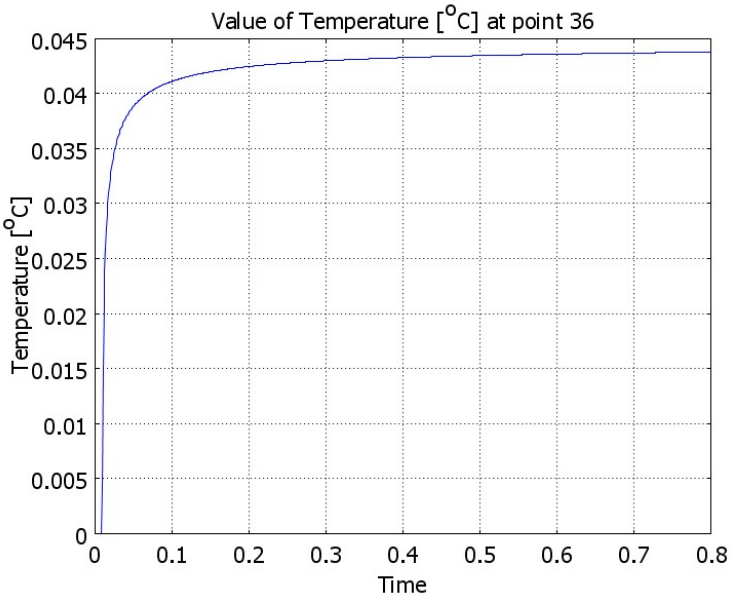


Figure E.4. 3D FEM simulation result for Design C4's rise time in water.

3D FEM simulation of heat transfer of Design C5 is shown in Figure E.5 and its simulation result in water is shown in Figure E.6. Rise time of Design C5 in water is 60 ms.

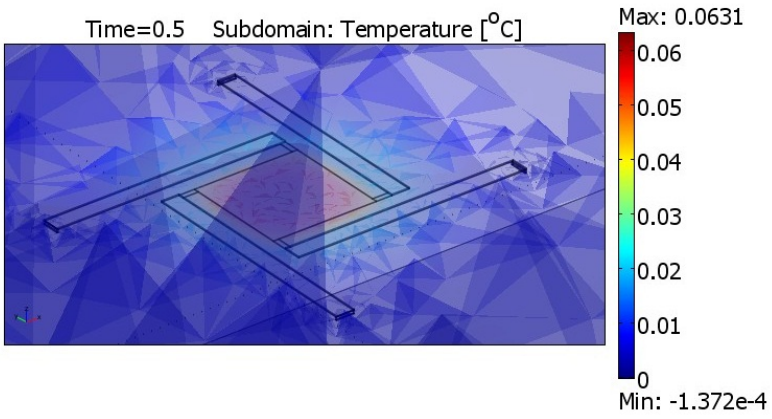


Figure E.5. 3D FEM for Design C5's rise time in water.

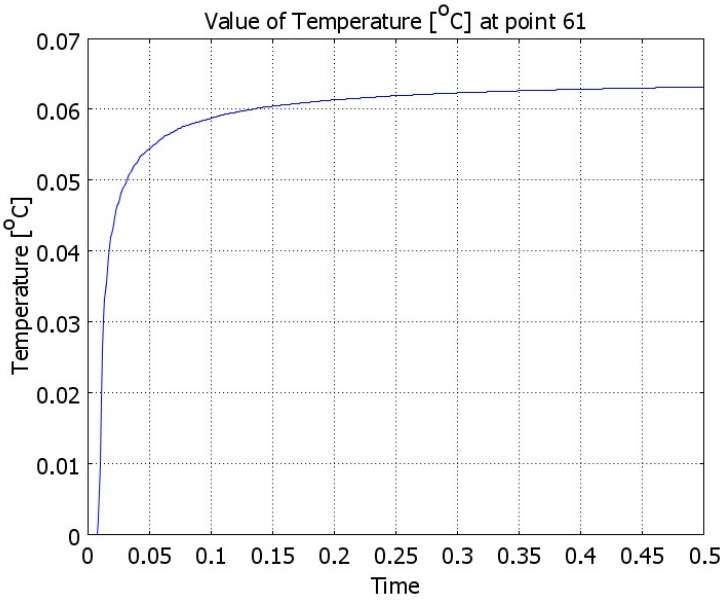


Figure E.6. 3D FEM simulation result for Design C5's rise time in water.

# APPENDIX F: STIFFNESS OF OTHER MICRO-STAGES

In the 3D FEM simulations to find the stiffness of the micro-stages, 1N force to the center point of the membranes is given and causes the micro-stages to deflect. Stiffness of the designed micro-stages that are calculated through the 3D FEM simulation results which are shown in Figures F.1, F.2, F.3, F.4 and F.5 below. Stiffness of Design C2, Design C3, Design C4, Design C5 and Design D2 are calculated from the simulation results as 0.497 N/m, 0.505 N/m, 0.303 N/m, 0.8 N/m and 0.921 N/m, respectively.

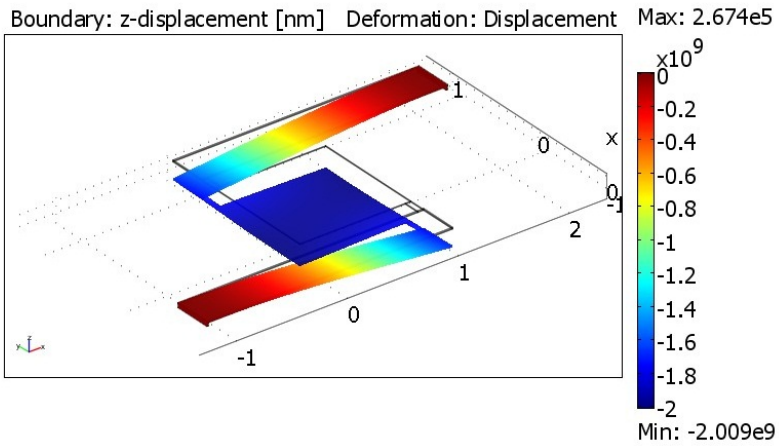


Figure F.1. Deflection result of Design C2 as 1N force is given to the center point.

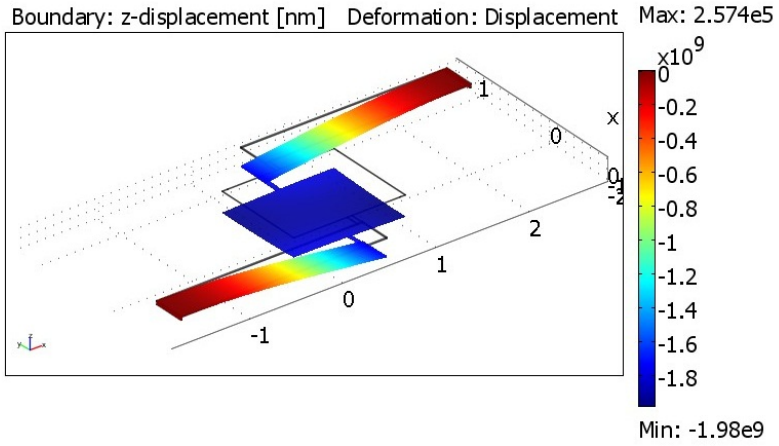


Figure F.2. Deflection result of Design C3 as 1N force is given to the center point.

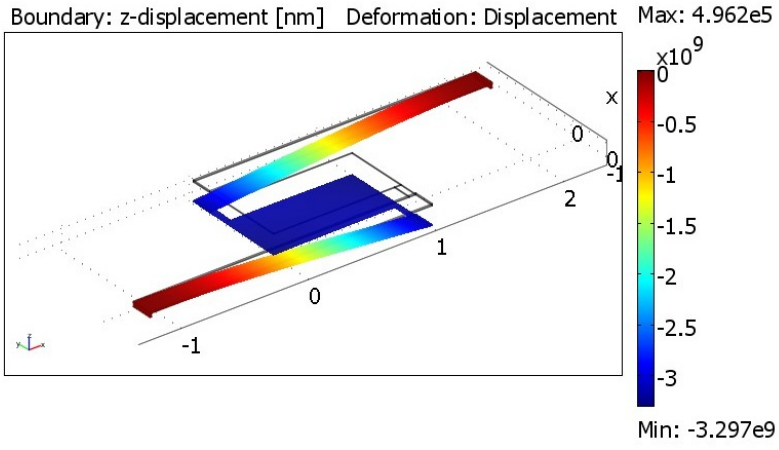


Figure F.3. Deflection result of Design C4 as 1N force is given to the center point.

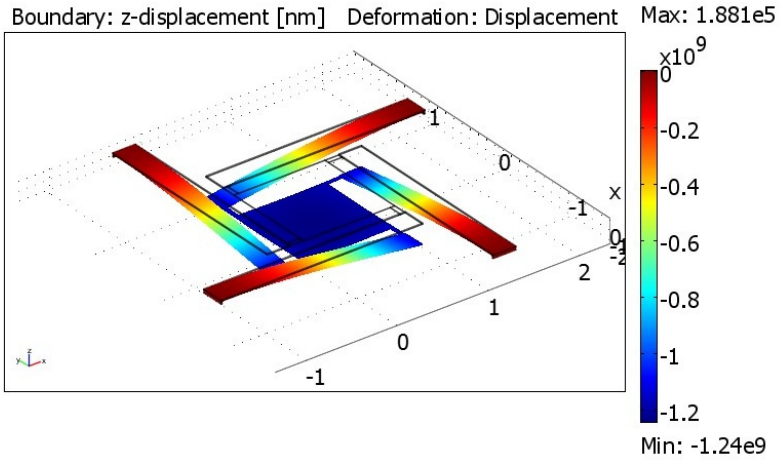


Figure F.4. Deflection result of Design C5 as 1N force is given to the center point.

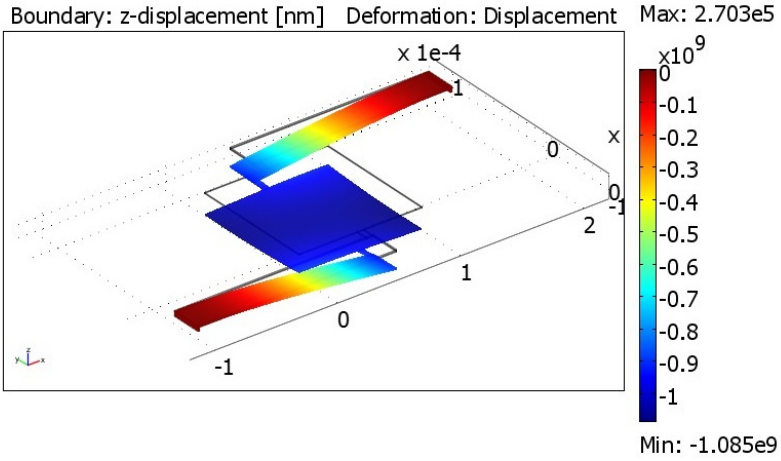


Figure F.5. Deflection result of Design D2 as 1N force is given to the center point.

# APPENDIX G: MASK LAYOUTS

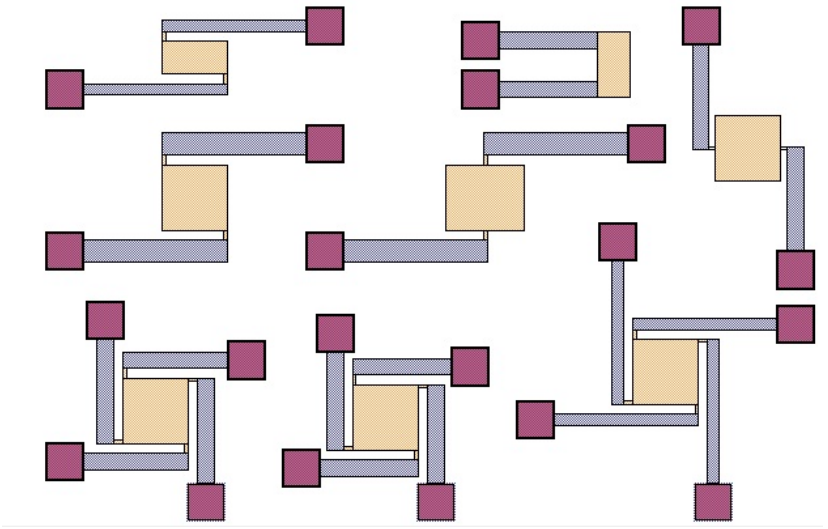

Figure G.1. Three layer of masks.

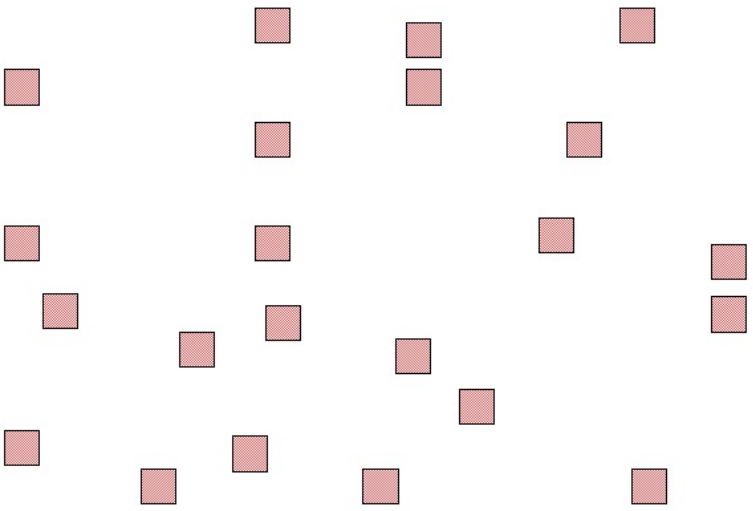

Figure G.2. First mask.

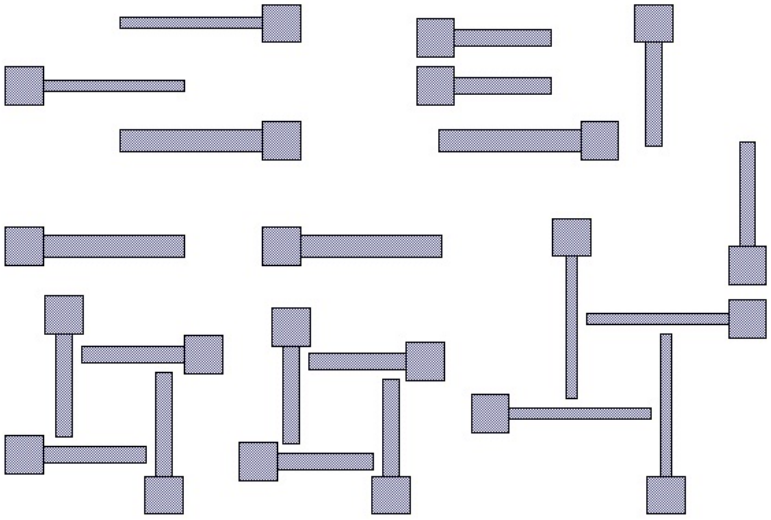

Figure G.3. Second mask.

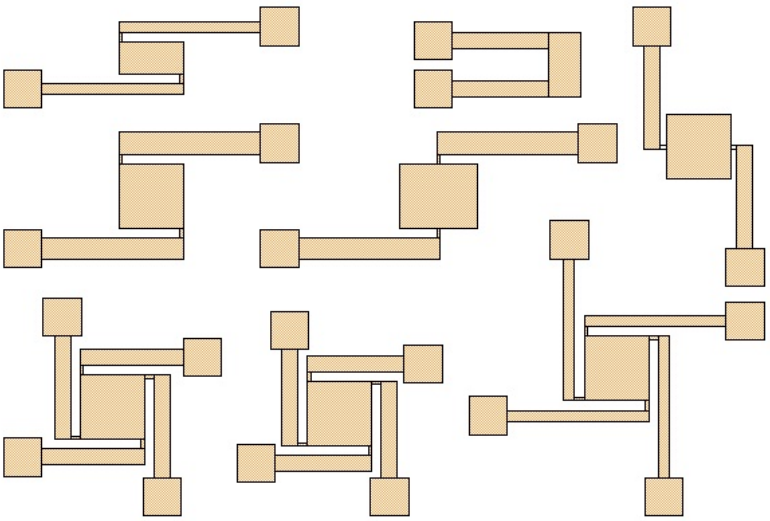

Figure G.4. Third mask.

# REFERENCES


1. Ashkin, A. and J. Dziedzic, "Optical Trapping and Manipulation of Viruses and Bacteria", *Science*, Vol. 235, No. 4795, p. 1517, 1987.

2. Bockelmann, U., P. Thomen, B. Essevaz-Roulet, V. Viasnoff and F. Heslot, "Unzipping DNA with Optical Tweezers: High Sequence Sensitivity and Force Flips", *Biophysical Journal*, Vol. 82, No. 3, pp. 1537–1553, 2002.

3. Bustamante, C., Z. Bryant and S. Smith, "Ten Years of Tension: Single-molecule DNA Mechanics", *NATURE-LONDON-*, pp. 423–426, 2003.

4. Fällman, E., S. Schedin, J. Jass, B. Uhlin and O. Axner, "The Unfolding of the P Pili Quaternary Structure by Stretching is Reversible, Not Plastic", *EMBO reports*, Vol. 6, No. 1, pp. 52–56, 2004.

5. Berry, R. and H. Berg, "Absence of a Barrier to Backwards Rotation of the Bacterial Flagellar Motor Demonstrated with Optical Tweezers", *Proceedings of the National Academy of Sciences*, Vol. 94, No. 26, p. 14433, 1997.

6. Neuman, K. and A. Nagy, "Single-molecule Force Spectroscopy: Optical Tweezers, Magnetic Tweezers and Atomic Force Microscopy", *Nature Methods*, Vol. 5, No. 6, pp. 491–505, 2008.

7. Lipfert, J., X. Hao and N. Dekker, "Quantitative Modeling and Optimization of Magnetic Tweezers", *Biophysical Journal*, Vol. 96, No. 12, pp. 5040–5049, 2009.

8. Gosse, C. and V. Croquette, "Magnetic Tweezers: Micromanipulation and Force Measurement at the Molecular Level", *Biophysical Journal*, Vol. 82, No. 6, pp. 3314–3329, 2002.

9. Conroy, R., "Force Spectroscopy with Optical and Magnetic Tweezers", *Handbook*

*of Molecular Force Spectroscopy*, pp. 23–96, 2008.

10. Owen, R., *A Practical Guide to AFM Force Spectroscopy and Data Analysis*, 2004.

11. Torun, H., O. Finkler and F. Degertekin, "Athermalization in Atomic Force Microscope Based Force Spectroscopy Using Matched Microstructure Coupling", *Review of Scientific Instruments*, Vol. 80, p. 076103, 2009.

12. Mokaberi, B. and A. Requicha, "Drift Compensation for Automatic Nanomanipulation with Scanning Probe Microscopes", *Automation Science and Engineering, IEEE Transactions on*, Vol. 3, No. 3, pp. 199–207, 2006.

13. Wang, Y., G. Li and L. Liu, "Local Scan for Compensation of Drift Contamination in AFM Based Nanomanipulation", *Intelligent Robots and Systems, 2009. IROS 2009. IEEE/RSJ International Conference on*, pp. 1345–1350, IEEE, 2009.

14. Wenzler, L., G. Moyes and T. Beebe, "Improvements to Atomic Force Microscopy Cantilevers for Increased Stability", *Review of Scientific Instruments*, Vol. 67, No. 12, pp. 4191–4197, 1996.

15. Beyder, A., C. Spagnoli and F. Sachs, "Reducing Probe Dependent Drift in Atomic Force Microscope With Symmetrically Supported Torsion Levers", *Review of Scientific Instruments*, Vol. 77, p. 056105, 2006.

16. Fan, L., D. Potter and T. Sulchek, "Constant Tip-surface Distance with Atomic Force Microscopy via Quality Factor Feedback", *Review of Scientific Instruments*, Vol. 83, No. 2, pp. 023706–023706, 2012.

17. Torun, H., *Micromachined Membrane-based Active Probes for Biomolecular Force Spectroscopy*, Ph.D. Thesis, Georgia Institute of Technology, 2010.

18. Zhao, Y., *Optomechanical Uncooled Infrared Imaging System*, Ph.D. Thesis, University of California, Berkeley, 2002.

19. Incropera, F., D. DeWitt, T. Bergman and A. Lavine, *Introduction to Heat Transfer*, Wiley, 2006.

20. Hillier, A. and A. Bard, "Ac-mode Atomic Force Microscope Imaging in Air and Solutions with a Thermally Driven Bimetallic Cantilever Probe", *Review of Scientific Instruments*, Vol. 68, p. 2082, 1997.

21. Williams, K. and R. Muller, "Etch Rates for Micromachining Processing", *Journal of Microelectromechanical Systems*, Vol. 5, No. 4, pp. 256–269, 1996.

22. William, K., K. Gupta and M. Wasilik, "Etch Rates For Micromachining Processing: Part II", *Journal of Microelectromechanical Systems*, Vol. 12, No. 6, pp. 761–778, 2003.

23. Ohler, B., "Practical Advice on the Determination of Cantilever Spring Constants", *Spring*, pp. 1–12, 2007.

24. Han, W. and F. Serry, "Force Spectroscopy with the Atomic Force Microscope", *Application Note of Agilent*.

25. Serry, F., "Improving the Accuracy of AFM Force Measurements: The Thermal Tune Solution to the Cantilever Spring Constant Problem", *Santa Barbara: Veeco Instruments Inc*, 2005.

26. Toda, M., T. Ono, F. Liu and I. Voiculescu, "Evaluation of Bimaterial Cantilever Beam for Heat Sensing at Atmospheric Pressure", *Review of Scientific Instruments*, Vol. 81, No. 5, p. 055104, 2010.